THREE DIMENSIONAL NANOPLASMONIC SURFACES: MODELING, FABRICATION AND CHARACTERIZATION

A THESIS
SUBMITTED TO THE DEPARTMENT OF ELECTRICAL AND
ELECTRONICS ENGINEERING
AND THE GRADUATE SCHOOL OF ENGINEERING AND SCIENCE
OF BILKENT UNIVERSITY
IN PARTIAL FULLFILMENT OF THE REQUIREMENTS
FOR THE DEGREE OF
MASTER OF SCIENCE

By
Kıvanç Güngör
January 2013

I certify that I have read this thesis and that in my opinion it is fully adequate, in scope and in quality, as a thesis for the degree of Master of Science.

—————————————————

Assoc. Prof. Dr. Hilmi Volkan Demir (Supervisor)

I certify that I have read this thesis and that in my opinion it is fully adequate, in scope and in quality, as a thesis for the degree of Master of Science.

—————————————————

Prof. Dr. Ayhan Altıntaş

I certify that I have read this thesis and that in my opinion it is fully adequate, in scope and in quality, as a thesis for the degree of Master of Science.

—————————————————

Assist. Prof. Dr. Mehmet Zeyyad Baykara

Approved for Graduate School of Engineering and Science

—————————————————

Prof. Dr. Levent Onural
Director of Graduate School of Engineering and Science

ii

ABSTRACT

THREE DIMENSIONAL NANOPLASMONIC SURFACES: MODELING, FABRICATION AND CHARACTERIZATION

Kıvanç Güngör
M.S. in Electrical and Electronics Engineering
Supervisor: Assoc. Prof. Dr. Hilmi Volkan Demir

January 2013

Today designing functional nanoplasmonic structures specific to a variety of applications attracts great interest from various fields ranging from optoelectronics to life sciences. There are numerous ways of making nanoplasmonic structures. Among them, nanopatterning of a thin-film metal layer is one of the most common approaches, which allows for finely controlled fabrication of a plasmonic unit and their repeating layout in the plane of the starting metal film. Although there are many examples of such nanopatterned plasmonic structures reported to date, they are typically designed and implemented on a planar surface. In these architectures, plasmonic layout commonly covers significantly less than 100% of the substrate surface and can provide field localization most strongly around the sharp corners and small gaps between the patterns. In the case of using a periodic layout, which is commonly employed for experimental realization (although periodicity is not necessary), the plasmonic array inherently yields a duty cycle substantially less than unity (usually close to 0.5). As a result, the surface coverage of nanopatterned plasmonic structures on a planar surface has intrinsically been limited and the field enhancement across their nanoplasmonic layout has been possible mostly in the plane and slightly above it. To address these limitations, this thesis proposed and demonstrated three-dimensional (3D) nanoplasmonic arrayed structures designed and implemented on a non-planar surface that allows for strong field enhancement in the out-of-plane direction and enables a very large surface coverage of the substrate close to unity. The thesis work included both

numerical modeling and experimental characterizations. As a proof-of-concept demonstration, we fabricated non-planar arrays of checkerboard nanostructures, each with two-fold rotational symmetry, laid out in a volumetric fashion as two interlocked square lattice arrays at two different levels, facilitating strong field localization vertically between these two complementary planes. The resulting nanofabricated samples exhibited a maximum surface coverage of 100% in plan view. With full electromagnetic solution of such 3D nanoplasmonic surfaces, we showed that the out-of-plane field localization is 7.2-fold stronger than the in-plane localization, in comparison to their two-dimensional (2D) components alone. These numerical results agree well with the experimental observations including far-field optical transmission and reflection measurements. The absorption spectroscopy further revealed that the resulting spectrum of the 3D checkerboard features a unique signature arising from the out-of-plane localization, which does not exist in the case of the 2D counterparts. These results indicate that 3D nanoplasmonics of such non-planar surfaces provides us with the ability to generate and better utilize the plasmonic volume, possibly useful for increased plasmonic coupling and interactions.

Keywords: Plasmonics, plasmonic nanostructures, FDTD simulation, nanofabrication

ÖZET

ÜÇ BOYUTLU PLAZMONİK YÜZEYLER: MODELLEME, NANOFABRİKASYON VE KARAKTERİZASYON

Kıvanç Güngör
Elektrik ve Elektronik Mühendisliği Bölümü Yüksek Lisans
Tez Yöneticisi: Doç. Dr. Hilmi Volkan Demir

Ocak 2013

Günümüzde çeşitli uygulama alanlarına özel işlevsel nanoplazmonik yapıların tasarımı optoelektronikten hayat bilimlere kadar farklı alanlardan ilgi çekmektedir. Nanoplazmonik yapıların çok sayıda üretim yolları olmakla birlikte ince bir metal film tabakasının nanoşekillendirilmesi en sık kullanılan yöntemlerden birisidir. Bu yaklaşım oldukça hassas bir şekilde yapılan plazmonik birim hücresinin üretimine ve bu hücrenin aynı hassasiyetle metal yüzeyde tekrarlanmasına dayanmaktadır. Bugüne kadar bu tür nanoplasmonik yapıların birçok örneği olmakla birlikte, bu yapılar genellikle düzlemsel bir yüzey üzerine tasarlanmış ve uygulanmıştır. Bu mimarilerde plazmonik yapı genellikle alttaş yüzeyinin %100'ünü kaplamaktan oldukça uzak olmakta ve elektrik alan keskin köşeler ile motifler arasındaki küçük gediklerde hapsedilebilmektedir. Bir zorunluluk olmasa da periyodik yapıların kullanımı deneysel gerçekleme için sıkça kullanılmaktadır ve bu yapıların yüzey kaplama oranları -genellikle yüzeyin yarısına yakın olup- tabiatları gereği tam kaplamadan çok daha azdır. Sonuç olarak, bir düzlemsel yüzey üzerinde üretilen nanoplasmonik yapıların yüzey kaplama oranları doğal olarak sınırlandırılmıştır ve bu yapıların elektrik alan artırımı çoğunlukla düzlemsel ya da hafifçe yapı üzerinde mümkün olmuştur. İşbu tezde, sıralanan sınırlamaları aşmak adına şiddetli alan artırımını yüzeye dik olarak sağlayabilen ve alttaş yüzeyini %100'e çok yakın bir oranla kaplayan üç boyutlu nanoplazmonik yapılar düzlemsel olmayan bir yüzey olarak tasarlanmış ve uygulanmıştır. Çalışmalarımız sayısal modelleme ve deneysel karakterizasyonu içermektedir. Tasarımımızın

çalışmasını kanıtlamak için üç boyutlu, düzlemsel olmayan ve 180 derece döndürme simetrisine sahip dama tahtası nanoyapıları ürettik. Belirtilen dama tahtası yapılarında birbirini tamamlayan iki kare örgü dizisi yüzeyleri belirli yükseklikle birbirinden ayrılmakta ve bu iki birbirini tamamlayan düzlem arasındaki ayrım oldukça güçlü bir alan artırımı sağlamaktadır. Üretilmiş yapılar kuşbakışı %100 oranla yüzeyi kaplamaktadır. Nanoplazmonik yapıların elektromanyetik çözümü üçboyutlu nanoplazmonik yüzeylerin yüzeye dik modlarının alan artırımının iki boyutlu bileşenlerinin düzlemsel alan artırımına göre 7,2 kat daha güçlü olduğunu göstermiştir. Elde edilen sayısal sonuçlar uzak-saha optik iletim ve yansıma ölçümleri içeren deneysel gözlemleri ile oldukça uyumlu çıkmıştır. Soğurma spektroskopisi ayrıca düzleme dik alan yoğunlaşmanın sonucu, iki boyutlu yapılarda gözlenmeyen, üç boyutlu yapılara has spektral imzayı ortaya çıkarmıştır. Bu sonuçlar gösteriyor ki üç boyutlu plazmonik yüzeyler, plazmonik etkileşimi hacimsel olarak artırarak bu etkileşimden daha iyi istifade etme olanağı sağlamaktadır.

Anahtar Kelimeler: Plazmonik, plazmonik nanoyapılar, zamanda sonlu farklar metodu (FDTD) benzetmesi, nanofabrikasyon.

Acknowledgements

When I first stepped into Prof. Hilmi Volkan Demir's office in July 2008, I could not imagine this day would come true. First of all I would like to thank Prof. Demir for accepting me as a M.S. student in Department of Electrical and Electronics Engineering while I was a graduate of Department of Physics. Through my M.S. studies I learned a lot from him. Without his motivational speeches and support, these years would be a lot more difficult.

I also would like to thank my thesis committee members Prof. Ayhan Altıntaş and Prof. Mehmet Z. Baykara for their interest in my thesis. Their useful and inspiring comments and feedbacks are invaluable. Prof. Ayhan Altıntaş was department chair when I applied to M.S. program and I also thank for his positive attitude during my application procedure.

Definitely the best part of being a member of Demir Group is working with its members. During my studies I learned lots of things from them. The support and friendship among the team is unique. I thank Emre Ünal for teaching almost everything about nanofabrication. I will remember our talks in cleanroom and EBL room. Özgün Akyüz made everything quite simple for us. Birsen Bilgili stuffed our stomach in every special occasion. Also office 306 team deserves a special thank for their support, patience and motivation during my research and while writing my thesis. I thank Yusuf Keleştemur for "well cooked" quantum dots, Ahmet Fatih Cihan for motivated time-resolved measurements, Burak Güzeltürk for his novel and crazy ideas, Hüseyin Cüneyt Eroğlu for good talks and discussions about life, Talha Erdem for his support, Can Uran for his smiling face, Halil Akçalı for accelerating us, İbrahim Akçalı for preventing Halil not to accelerate too much, Shahab Akhavan for showing the extreme point of everything, Aydan Yeltik for her warnings about being "positive", Ozan Yerli for keeping our server "up" and dealing every digital thing in our group and Dr. Evren Mutlugün for motivational speeches. I also thank Dr. Nihan

Kosku Perkgöz, Dr. Pedro Ludwig Hernandez-Martinez, Dr. Vijay Kumar Sharma, Ersin Doğan, Onur Akın, Veli Tayfun Kılıç, Sayim Gökyar, Akbar Alipour, Mehmet Zafer Akgül, Onur Erdem and Berkay Bozok along with all Demir Group alumni.

All UNAM administrative and technical staff especially Mustafa Güler, Adem Saraç and Semih Yaşar made everything easy and kept everything up. Mürüvet Parlakay in Department of Electrical and Electronics Engineering made every administrative procedure just simpler. I thank you all.

My special thanks go to Yasemin Kara who made my last five years full of happiness. I miss our undergraduate years a lot, yet too excited to see forthcoming years. With her everything is much easier, joyful, and bearable. I am fortunate to have her.

Finally, there is no way I can truly show my gratitude to my parents -Aynur and Mehmet- and my little brother İnanç. Their devotion for my education and needs cannot be compensated. I thank them a lot and dedicate this thesis to them. I especially thank my brother for being main source of humor in my life.

Table of Contents

List of Figures

List of Tables

To my parents and brother,

"They were always present when I need them."

Chapter 1

Introduction

Both physical and chemical properties of bulk materials change significantly when the particle sizes reduce down to nanometer scale. Generally change in the optical properties is correlated with the absorption behavior. Both chemical and optical properties are determined mainly by valence electrons. Quantum confinement of electrons changes electron energy levels significantly.

The first known example of plasmonic metal nanoparticle usage is the Lycurgus Cup made the in 4th century AD in the name of Lycurgus, a king of Thracians, shown in Figure 1.1. It is quite common (and almost unavoidable) among the plasmonics community to start introducing the plasmonics with this historical cup having dichroic glass properties. Colloidal silver and gold nanoparticles in the glass scatter the green light more which causes the observed green color when illuminated from outside and red with the illumination from inside.

Especially for the past last twenty years, plasmonic applications attract interest from various fields ranging from optoelectronics to life sciences [1–3]. Localized surface plasmons (LSPs) are collective oscillations of electrons under impinging electromagnetic radiation. Metals such as gold, silver and copper

sustain surface plasmons in the visible wavelength region due to their d shell interband electronic contributions [4]. Controlling the size, shape and periodicity of metallic nanoparticles, it is further possible to tailor the resonance frequency of the structure specific to a targeted application. Number of studies reported extraordinary light transmission [5], enhanced absorption for photovoltaic applications [6], two-photon absorption luminescence from noble metals [7], [8], refractive index sensing [9] and surface enhanced Raman spectroscopy (SERS) applications [10–13] as well as fluorescence enhancement of quantum dots [14–20] and dyes [21].

Illumination from outside   Illumination from inside

Figure 1.1. The Lycurgus Cup was made in the 4th century AD. Embedded metal nanoparticles give distinct optical properties to the cup. Illuminations from outside and inside change the color of the structure. © Trustees of the British Museum [22]**.**

In case of SERS applications of plasmonic structures, enhancement generally depends on the fourth power of the incident electric field amplitude [23] neglecting the density of states contribution [24]. However, photoluminescence

2

(PL) enhancement of semiconductor quantum dots (QDs) includes two competitive effects. While exploiting the near-field enhancement of plasmonic structure, fluorescence enhancement of QDs suffers from quenching effect in the close proximity of metals [14–16]. To observe fluorescence enhancement, QDs should be placed at an optimum point without quenching effect dominating or near-field enhancement vanishing.

Although there are applications of SERS using 3D plasmonic structures [10], [12], [13] in the literature, there are only planar 2D plasmonic structures providing fluorescence enhancement in the literature [18–21]. 2D structures have surface coverage of less than unity, while 3D structures can facilitate fluorescence enhancement all over the surface with additional out-of-plane coupling modes.

1.1 Motivation

As we discussed in the previous section, in the literature there are examples of two dimensional plasmonic structures. However, they lack enhancement in a volumetric fashion and also their surface coverage is inevitably less than unity. The main motivation behind three dimensional plasmonc structures is to take advantage of overall surface enhancement having hundred percent surface coverage. With just an interplanar spacing between two complementary plasmonic planes, it is possible to create coupling and field electric field intensity enhancement in the out-of-plane direction providing another degree of freedom to tune the plasmonic resonance frequency.

Field enhancement of 2D structures occurs very close to the surface restricting that an emitter layer must be very thin and close to the surface in order to exploit the electric field enhancement on the surface. With a volumetric field intensity enhancement mechanism, 3D structures can be the solution for this problem especially for thick emitter layers. As being tunable and low cost materials, QDs

are quite important for optoelectronic and photonic applications. Some of the applications of QDs include solar cells [25], [26], light-emitting diodes [27] and lasers [28]. However, one of the main problems with the applications of QD devices is the reduced film quantum efficiencies of QDs. Plasmonically coupled QDs can overcome this problem in terms of emission and absorption enhancement processes.

1.2 Thesis Structure

This thesis work is organized as follows:

In Chapter 1 we introduced the concepts in this study by giving examples from the literature. Motivation behind using three dimensional structures is discussed briefly.

Chapter 2 deals with the scientific background of surface plasmons under two different types as surface plasmon polaritons and localized surface plasmons, which have quite different responses and properties. Then, brief information about nanocrystal quantum dots and their differences with bulk materials are stated.

In Chapter 3, the theoretical study part of the thesis work is presented. Simulation results are discussed for 2D and 3D structure differences. Periodicity effects on 2D and 3D structures are investigated by their grating counterpart. Also, we looked for two components of 3D structure and compared their overall effect with 3D structure to observe the coupling effects between the planes. The simulated field maps and electric field enhancement factors are used to compare measured enhancement factors from the experimental data.

In Chapter 4 we provided the experimental background information in terms of fabrication and characterization methods. First, the fabrication methods used in

this work are described considering important aspects and parameters. Then, the fabrication steps with the used parameters are given in detail. Characterization methods are divided as the structural and optical characterization methods. Similarly, explaining the utilized tools is followed by the experimental measurement results. After comparison of 2D and 3D structures, plasmonic responses in terms of optical measurements are given.

Chapter 2

Scientific Background

2.1 Theory of Surface Plasmons

Plasmon is the quanta of collective oscillations of electrons in a medium. In metals, valence electrons can move almost freely due to screened ionic potentials via core electrons. There are two types of plasmonic responses categorized as surface plasmon polaritons and localized surface plasmons. While surface plasmon polaritons can confine incoming electromagnetic radiation to sub-nanometer region within dielectric-metal interface and propagate in μm range [29], localized surface plasmons are bound to an isolated particle and works as very efficient scatterers.

2.1.1 Surface Plasmon Polaritons

In Drude model, loosely bounded electrons can be regarded as free electron gas in metals. Under certain excitation conditions, displacing an electron gas in a volume will create a localized electric field, which will lead to a restoring force. Solving equation of motion under this restoring force condition, we obtain simple harmonic oscillation of free electron gas with resonance frequency called

plasma frequency or volume plasmon frequency. Volume plasmon frequency for free electron gas is given by

$$\omega_p^2 = \frac{ne^2}{\epsilon_0 m^*} \tag{1}$$

where n is the electron number density, e is the electron charge, ϵ_0 is free space dielectric constant, and m^* is the electron effective mass [30]. Note that, during the calculation of free electron gas model, there is no use of quantum mechanics and this approach is entirely classical. Crystal contribution and quantum mechanical effects on electrons are summed under effective mass value of electron as well as the electron number density n. Oscillation of free electron gas has longitudinal wave nature and cannot couple to electromagnetic waves having transverse wave nature. It is important that free electron gas oscillations occur in a volumetric fashion and because of this fact they can be called as volume plasmon waves in contrast to surface plasmon waves.

Surface plasmon waves are the result of translational symmetry breakdown at the surface. As a simple approach we can express the surface plasmon modes by the sum rule [31]. If we divide an infinitely large metal into two parts by an infinite plane, we obtain two infinite surfaces as illustrated in Figure 2.1.1.1. Sum rule states that squares of surface plasmon resonances of a void in bulk metal (ω_1^2) and a localized metal particle (ω_2^2) equals to the square of volume plasmon resonance frequency (ω_p^2):

$$\omega_1^2 + \omega_2^2 = \omega_p^2. \tag{2}$$

Using sum rule, we can find the surface plasmon resonance frequency by treating the metal having infinite volume composed of two parts separated by an infinite plane as shown in Figure 2.1.1.1. Then, we obtain $2\omega_{sp}^2 = \omega_p^2$ which

gives the surface plasmon resonance of metal-air interface $\omega_{sp} = \omega_p/\sqrt{2}$. This result is a simplified solution of metal-dielectric interface surface plasmon resonance frequency given by

$$\omega_{SP} = \omega_P/\sqrt{1 + \epsilon_d},$$

(3)

where ϵ_d is the dielectric constant of dielectric interface. Since $\epsilon_{air} \cong 1$, the sum rule solution is verified. Surface plasmon frequency is obtained from the continuity equation on the metal-dielectric interface in the long wave vector regime under TM wave excitation.
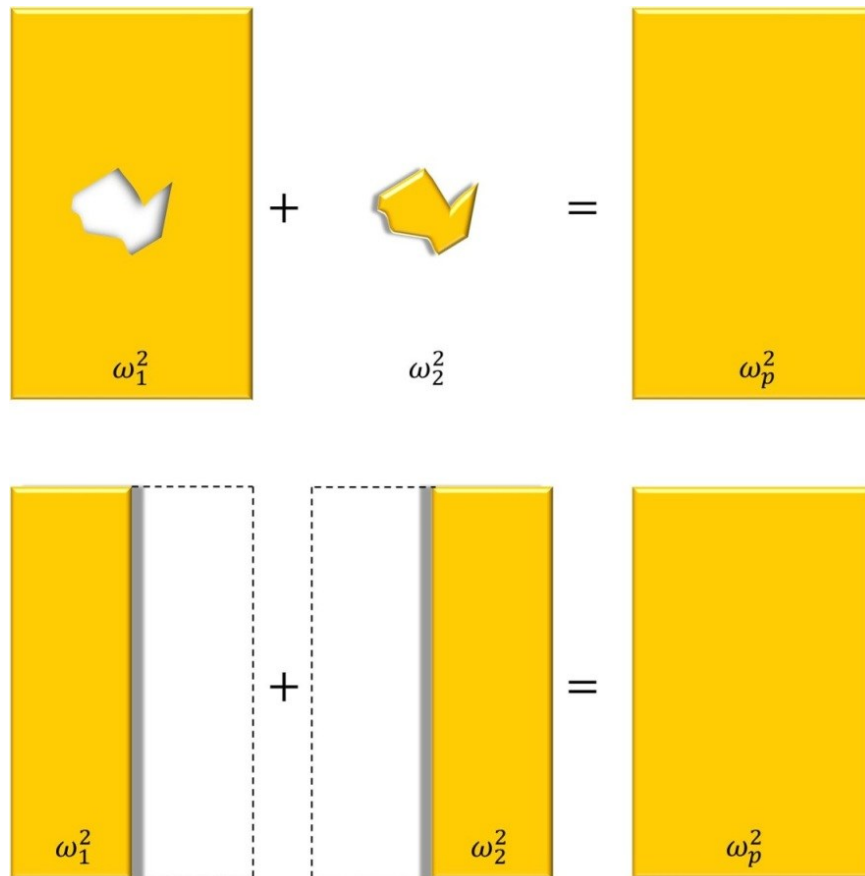
Figure 2.1.1.1 Sum rule for particle and void plasmons is illustrated (top). Similarly, sum rule for surface plasmon resonance at metal-air interface and its relation with volume plasmon resonance is illustrated (bottom).

Since ω_{sp} is a long wave vector solution, it can be treated as highly localized standing wave solution for surface plasmon polaritons. Surface plasmon polariton is namely the interaction of a plasmon and a photon. Like every polariton, it has a dispersion curve (Figure 2.1.1.2). Plasmon polariton dispersion curve is quite similar to the phonon polariton curve. While bulk volume plasmon branch is similar to the longitudinal optical phonon branch, the surface plasmon branch has the form and the behavior of the transverse optical phonon branch. Because of the longitudinal nature of volume plasmons, they cannot be coupled to optical excitations; they are observed in electron energy loss spectroscopy experiments [32].
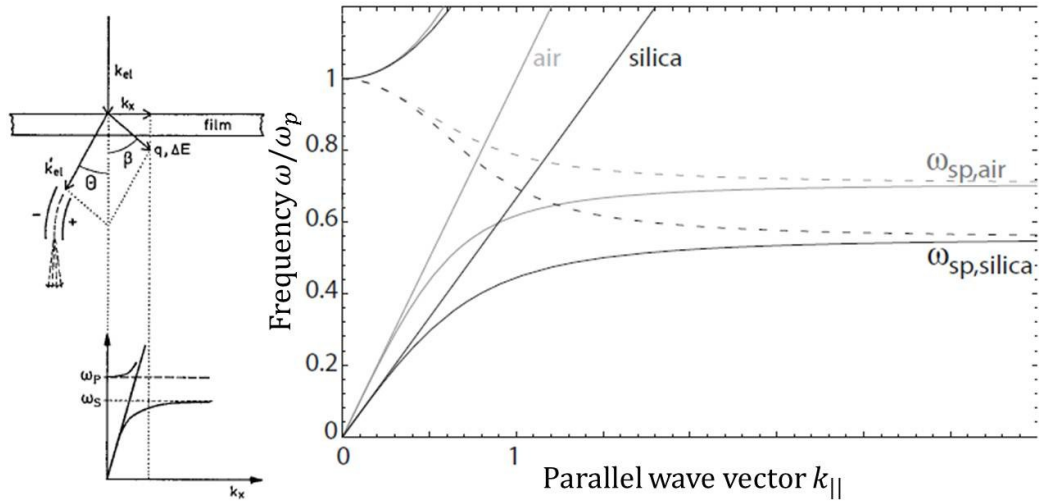
Figure 2.1.1.2. (Left) Relation of the plasmon polariton excitation geometry and surface plasmon polariton dispersion (after [33]). (Right) Detailed dispersion relation shows the dependence of surface plasmon frequency on the environmental dependence (reproduced after [29]). Note that frequency is normalized with respect to ω_p.

Using the obtained volume plasmon frequency, dielectric function of a metal in the Drude picture with characteristic electron collision frequency gives

$$\epsilon(\omega) = \epsilon_\infty - \frac{\omega_p^2}{\omega^2 + i\gamma\omega}. \qquad (4)$$
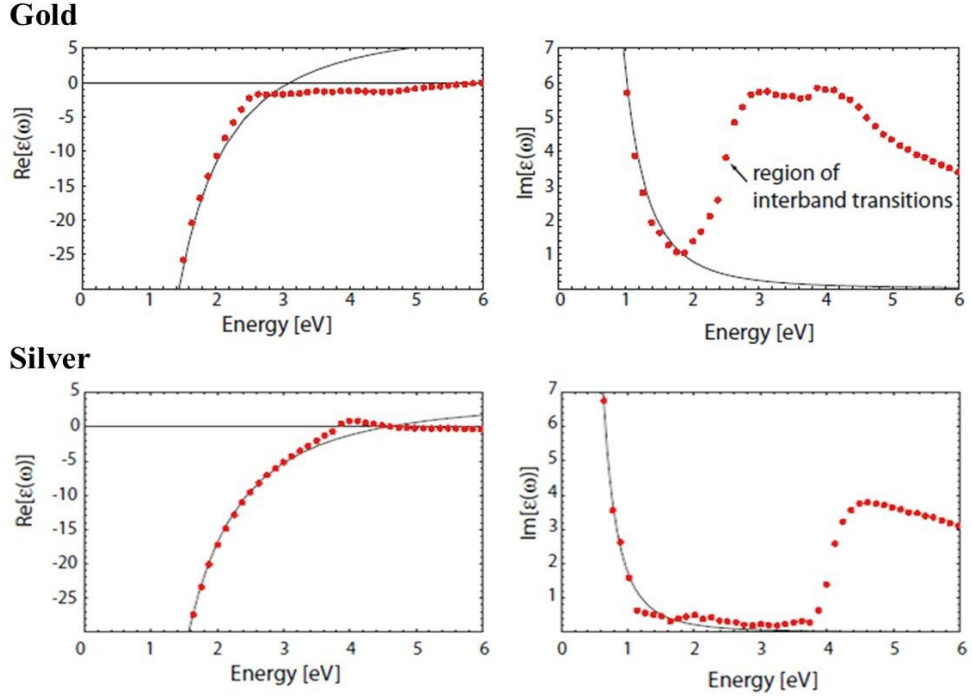
Gold

Silver

Figure 2.1.1.3. Real and imaginary parts of dielectric functions for gold and silver. Solid curve presents the Drude model calculations and dotted data points are experimental results. Discrepancy occurring at higher energies is due to contribution of d shell electrons in gold and silver to the conductivity. After [29].

Note that the dashed lines in Figure 2.1.1.3 correspond to pure imaginary solutions of parallel wave vector, which gives decaying wave solutions. Also, the group velocity in that region is negative, implying that light propagates backwards as it enters the metal. In real metals, other effects can contribute to the plasmonic response. In noble metals like gold and silver, d-band electrons contribute to the volume plasmon frequency above certain frequencies and create discrepancy in the Drude model as shown in Figure 2.1.1.3. These interband transitions make the gold and silver perfect candidates for visible region plasmonic applications. All the contributions to the Drude model are added using Lorentz oscillator model in the form of Lorentzian as

$$\epsilon_n(\omega) = \frac{C_n}{\omega_n^2 - \omega^2 - i\gamma_n\omega}. \tag{5}$$

Here we stated the nth resonance with the resonance frequency ω_n, the amplitude C_n and the collision frequency γ_n.

2.1.2 Localized Surface Plasmons

In the case of localized surface plasmons, collective oscillations of electrons are spatially confined in a medium as illustrated in Figure 2.1.2.1. Unlike the propagating surface plasmon polaritons, localized surface plasmons are bounded to a nanometer sized metal particle and can be excited in almost any illumination condition with a matching resonance frequency. Localized surface plasmons are analytically solved by Mie in 1908 [34] for spherical particles and modified version for the ellipsoid is also available [35].
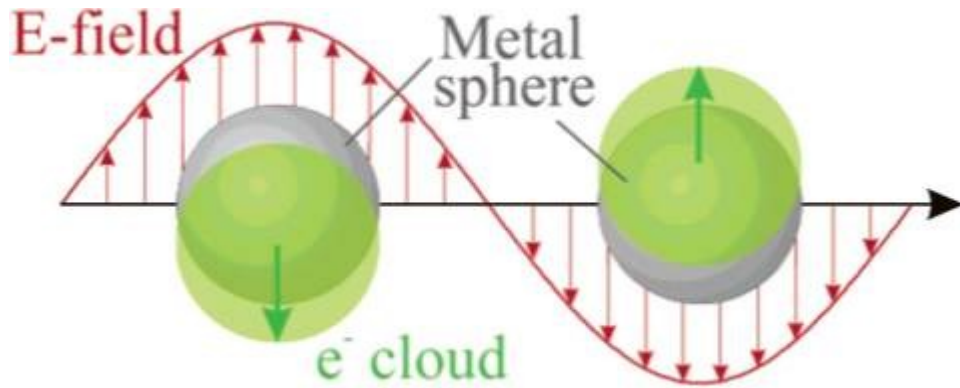
Figure 2.1.2.1. Collective oscillation of electrons in a metal sphere with the effect of incident electric field under quasi-static approximation. After [36]**.**

If the particle is smaller than the skin depth, electrons see almost no retardation effect or loss during their oscillation [29], [37]. With the increasing particle size, the retardation effects become effective and the resonance peak full width at half maximum (FWHM) increases so the quality factor of the oscillation decrease as shown in Figure 2.1.2.2. Quality factor (Q) is defined as

$$Q = \frac{f_0}{\Delta f} \tag{6}$$

where f_0 is the center frequency of resonance peak and Δf is the FWHM value of the resonance peak.
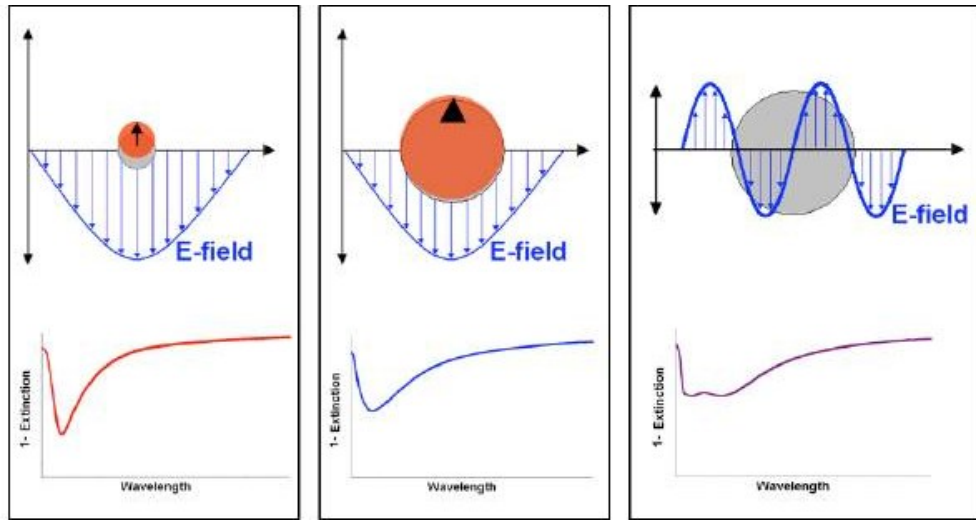
Figure 2.1.2.2. Validity region of the quasi-static approximation and its effect on the plasmonic resonance: a) Sharp peak occurs when incident wavelength is considerably larger than the particle. b) Damping mechanisms broaden the plasmonic resonance peak. c) When particle is larger than the wavelength, two or more peaks can be seen. After [38]**.**

For particles rather than the sphere or the ellipsoids, electrons can oscillate without any symmetry around an axis. Without any analytical calculation is present, numerical solutions are used to calculate the optical response of these particles. As an example, plasmonic nanowires distinctly show two extinction peaks. Blue-shifted one corresponds to smaller dimension (radius of the cylinder), which is known as transverse mode, and red-shifted resonance corresponds to longer dimension, which is called as longitudinal mode [39]. Similarly with more complex shapes, resonance wavelengths change dramatically.

An important figure-of-merit for the plasmonic structures is their extinction efficiencies. Extinction is defined as the sum of absorbed and scattered portions of the incident beam. While optical absorption process is effective for small particles, scattering becomes important for larger particles. Both of these mechanisms occur near the plasmonic resonance frequency. While considering our experimental and simulation results, we used the term percent absorptance

as summation of the effects of scattering and absorption processes. We calculated the absorptance (A) as

$$A = 100 - R - T, \qquad (7)$$

where R is the percent reflectance and T is the percent transmittance. The effect of the size and the shape of the nanoparticles on the scattering intensity is shown in Figure 2.1.2.3.
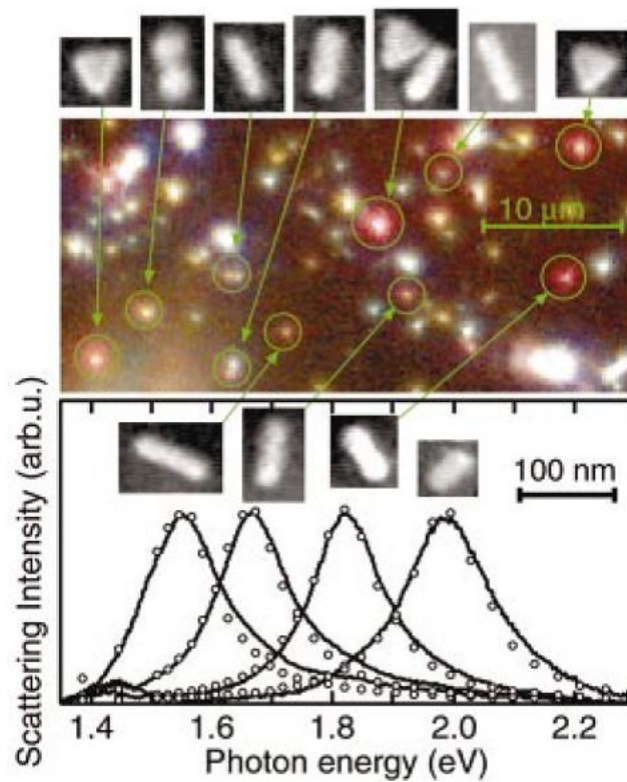
Figure 2.1.2.3. Size and shape dependence of the gold nanoparticles. For gold nanorods, spectra are taken with the polarizations along the long axis. Due to the damping mechanisms, higher aspect ratio results in energy red-shift. After [40]**.**

2.2 Colloidal Quantum Dots

We stated earlier that the quantum confinement of electrons in nanometer sized materials changes the response significantly with respect to their bulk behavior. Quantum confinement in one dimension creates quantum wells, that in two

dimensions create quantum wires, and that in three dimensions create quantum dots. While density of states a has square root of energy dependence above the band gap for bulk semiconductors, the picture changes to delta functions at the specific energy levels for QDs [41].
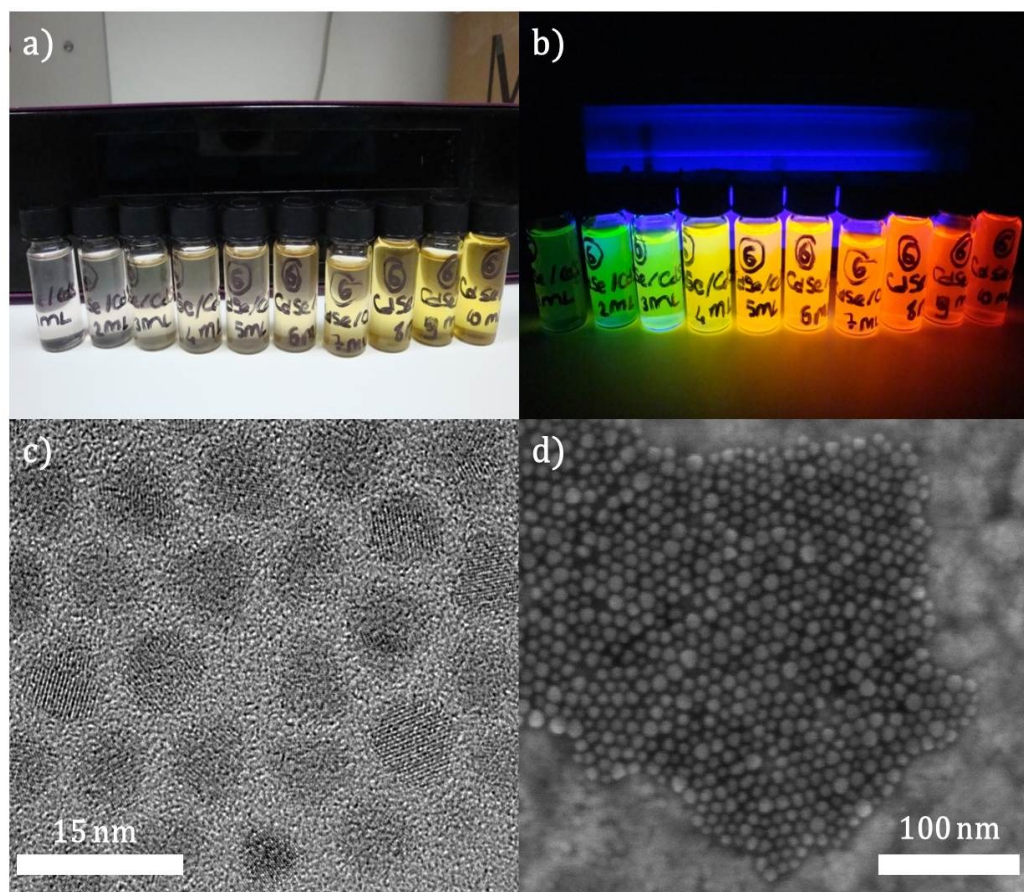
Figure 2.2.1. Giant QDs used in this work synthesized at our lab with various shell thicknesses without UV lighting (a) and under UV illumination (b). TEM images of 10 ML giant QDs (c). The size of giant QDs is sufficiently large even for SEM imaging (d).

QDs used in this thesis are CdSe/CdS core/shell structures synthesized at our lab. QDs with 10 monolayer shell known as "Giant" QDs having suppressed blinking and photobleaching properties, which are synthesized at our lab with the recipe from literature [42]. Giant QDs are large as they can be imaged using scanning electron microscopy (Figure 2.2.1.d). Their emission wavelength tunability comes from either core size variation or shell thickness differences.

As the core size decreases, the confinement of electrons increases, which further pushes the energy levels apart like particle-in-a-box solution of quantum mechanics, resulting in decreased emission wavelength. Similarly, increasing the shell thickness causes electrons to tunnel into the shell region, which reduces the confinement effect, hence increasing the emission wavelength of QDs as shown in Figure 2.2.1.a-b and Figure 2.2.2.
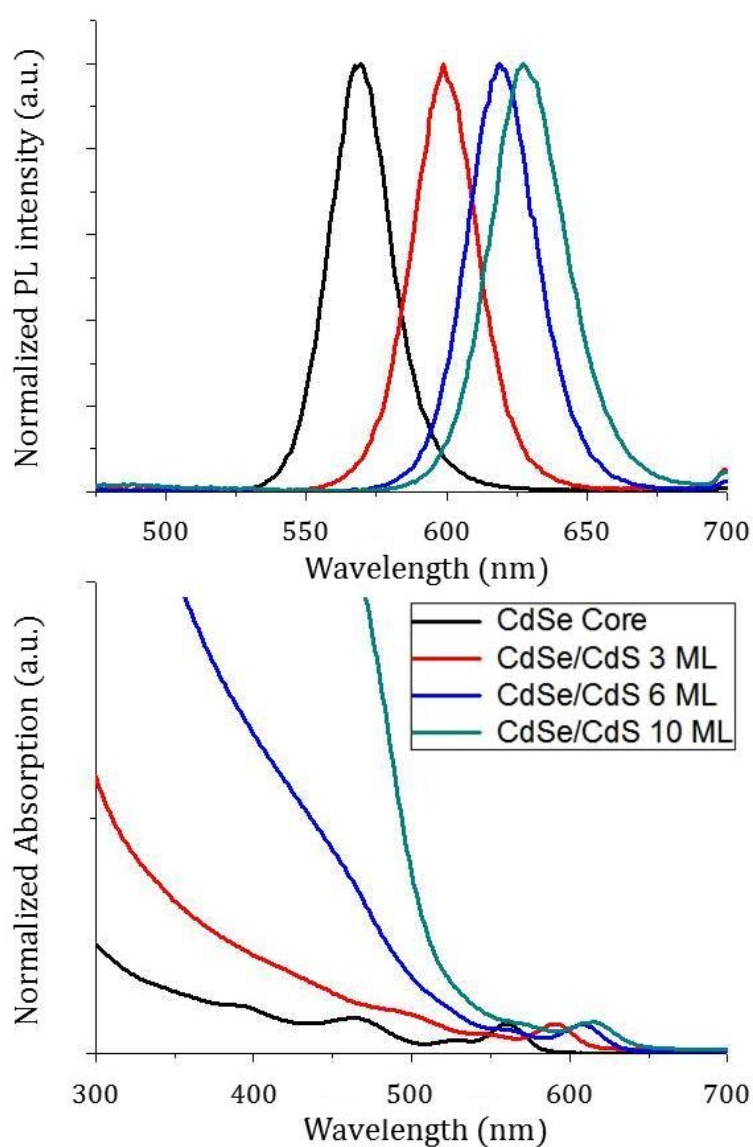
Figure 2.2.2. Normalized photoluminescence intensity (top) and normalized absorbance of our giant QDs with various shell thicknesses.

Chapter 3

Theoretical study

Theoretical understanding of the plasmonic structures is commonly limited in terms of the available pure analytical solutions. Only spherical (ellipsoids with some modifications) nanoparticles [34] and gratings [29] can be solved fully analytically. Because of this limitation, numerical solution methods are extensively used in the plasmonic calculations. In order to understand the plasmonic response, spatial electric field intensity distributions and absorption maps are used, which are not easy to measure from real fabricated devices. Also playing with the structure parameters, tailoring the desired properties requires less time and effort (and project funding) in the case of numerical simulations. Most commonly used methods include full-wave finite difference time domain (FDTD) [6], [43], [44], method of moments (MoM) [45] and discrete dipole approximation (DDA) [46], [47]. In this work, we used commercially available FDTD solver called FDTD Solutions, from Lumerical Inc.

FDTD method simply divides the simulation volume into small brick meshes and solves Maxwell equations numerically in defined small time steps. By taking Fourier transformations, we can obtain both temporal and spectral response (both in the nearfield and farfield) of the desired design under different excitations. Material data and its polynomial fit define the each material in the

simulations. Entering the structure and excitation geometry completes the general simulation setup. As a final remark, the boundary conditions and mesh sizes have to be taken into account considering the simulation cost and computational power available. We ran our simulations using 12 core Xeon processors with 24 GB available RAM.

3.2 Simulation Setup

Material data for gold, chromium and aluminum oxide is obtained using ellipsometry measurements. Measurements are made from a similar structure to provide reliability using chromium, gold and aluminum oxide coated on fused silica. All coatings are made with the exactly same method using during the fabrication of the structures of interest in this study. PMMA is taken as a constant dielectric with an index of refraction at 1.485 which, is well matched with the measured values on 3D structure. Material data used in this work are shown in Figure 3.2.1 for gold and Figure 3.2.2 for aluminum oxide and chromium. In order to avoid the polynomial fitting errors in material data fitting, we worked with single wavelength simulations with 5 nm wavelength steps.
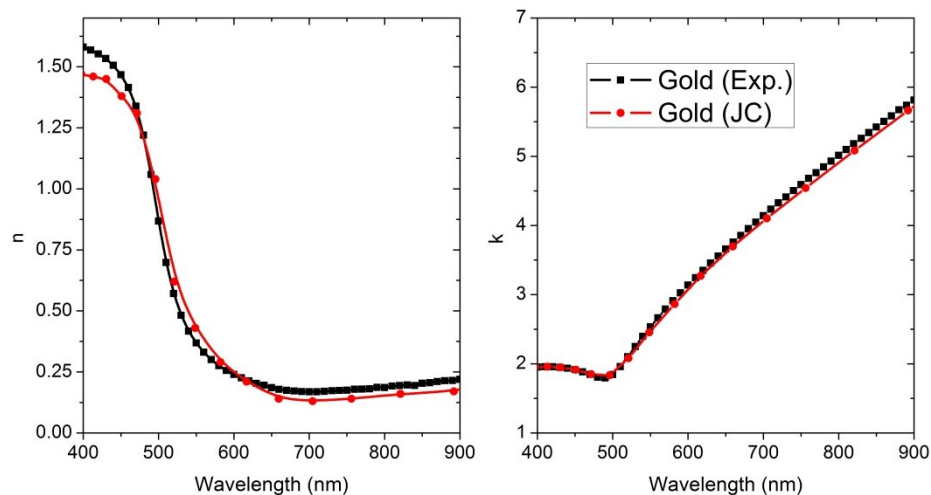
Figure 3.2.1. Real (n) and imaginary (k) part of the complex refractive index for gold. Data obtained from our ellipsometry measurements (black squares) and from literature (red circles) [48] **matches well.**
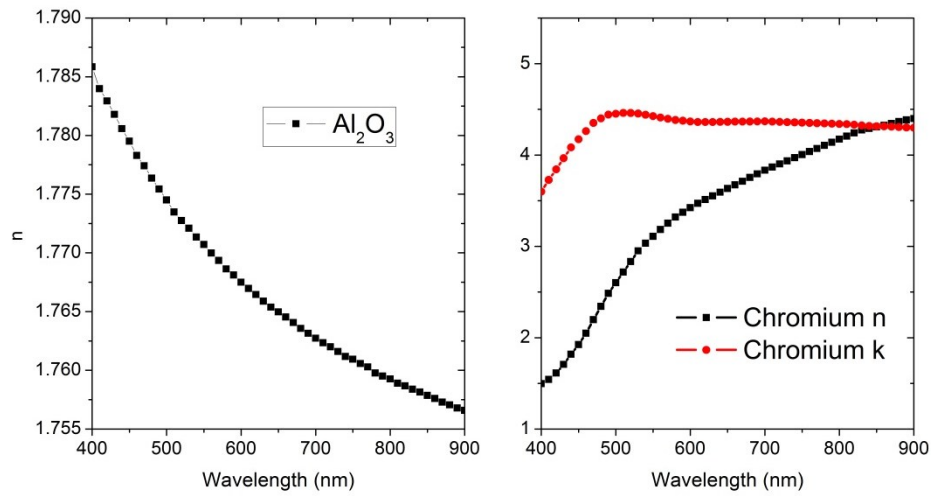
Figure 3.2.2. Complex refractive index for Al₂O₃ (left). Real (n) and imaginary (k) parts index for chromium (right). Data obtained from our ellipsometry measurements.
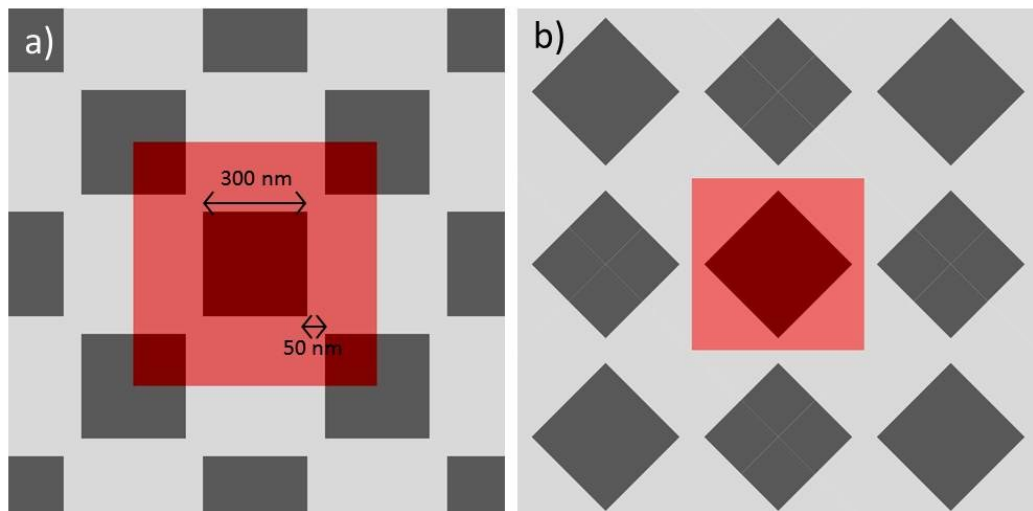
Figure 3.2.3. a) Conventional unit cell for checkerboard structure indicated with red square. Lateral gap is 50 nm between the repeating squares having 300 nm side length. b) Simulation unit cell diagonally aligned in order to exploit symmetrical BCs.

In addition to the translational symmetry of the checkerboard structure, two-fold rotational symmetry makes it possible to use symmetric and anti-symmetric boundary conditions (BCs) in the software. Symmetric BC is defined at the parallel plane of incoming electric field polarization and anti-symmetric BC is

defined orthogonal to the symmetric BC. This option reduces the computational power requirements four times with respect to the conventional periodic BCs for any periodic structure with translational symmetry. Simulation region is defined as 490 nm x 490 nm x 2 μm, noting that 350 nm periodicity of the structure corresponds to 494.98 nm in diagonal direction, which is taken as 490 nm considering uniform meshing as indicated with red square in Figure 3.2.3. In order to intersect the structure with the meshing, we placed a mesh override region on the structure with 2.5 nm x 2.5 nm x 2.5 nm cubical meshes. Careful convergence checks are made by reducing the mesh sizes as shown in Figure 3.2.4. We also used mesh override region with 1 nm^3 cubical meshes and compared its results with those of (2.5 nm)^3 meshing, which shows general far field agreement. Although there are some variations, general behavior holds true between the two meshing sizes. Cubical structures in our architecture can impose singularities at the corners, which can cause unphysical high electric field intensity increases. Reduced mesh size increases the local field enhancement at these points enormously while leaving unchanged the far field response since these localized points have negligible volume when integrating overall extinction. However, it is worth to mention that 1 nm^3 meshing takes approximately 11 hours to complete a single wavelength simulation whereas (2.5 nm)^3 meshed simulation configuration finishes within 7 minutes. The computation complexity thus motivated us to use (2.5 nm)^3 meshing.
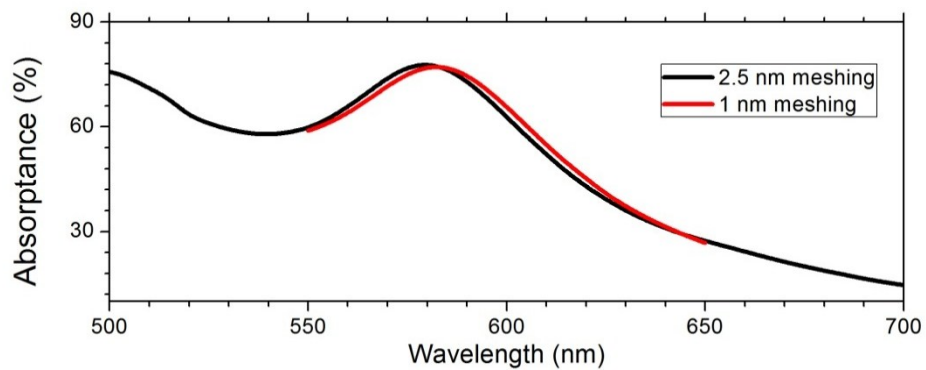
Figure 3.2.4. Convergence check for two different cubical mesh sizes. Although there are some differences between two mesh configurations, general trends are in good agreement.

In electron beam lithography technique, because of the interaction between the sample and the electron beam, outside of the scanned pattern never receives zero radiation. This effect is known as proximity effect and causes smoothing at sharp cornered features. In addition to the proximity effect, our O_2 plasma cleaning step adds additional smoothening to our structure. During the simulations, we considered this effect and instead of using unrealistic perfect cubes, we used rounded polygons, which model the corners with a circle having 40 nm radius.

In the simulations, extinction calculation is made using two 2D power field monitors along x-y plane. One monitor placed after the source gives the reflected wave data and the one placed after the structure in the silica gives the transmitted portion of the incoming wave. By obtaining the normalized transmitted data, it is possible to calculate the extinction by subtracting reflected and transmitted portions from unity. Also the electric field intensity profile maps are extracted using 3D field monitors.

3.3 Comparison: 2D - 3D Checkerboard Structure

After setting up simulation for the checkerboard architecture with 300 nm side lengths having 50 nm horizontal and vertical gaps between two adjacent square corners as shown in Figure 3.2.3, we obtained electric field intensity maps for the 3D and 2D checkerboards in Figure 3.3.1 having color scale in the logarithmic scale. Purpose of the logarithmic scale is to reduce the large contrast between hot spots (having intensity above 100 times larger than the incident excitation) and the volumetric field intensities with enhancement factors of around 10. As shown in the figure, we excite the structure with a plane wave source in the -z direction with the polarization along x direction having unity intensity in all wavelengths corresponding to 0 in the logarithmic scale. Simulated unit cell is indicated with the red square in the middle placed under x-z and y-z plane maps for both structures. For each structure field maps, x-z and

y-z planes are parallel and perpendicular to the source polarization, respectively. Four equally spaced x-y plane maps correspond to critical z values of the structure as shown in the cross-sectional side view in the middle: z=5 nm is the starting point of the structure, just above the chromium layer, z=45 nm is the top of the lower gold plane (corresponding to 2D structure without PMMA pillars around it), z=85 nm is the top of the PMMA layers and the bottom of the upper gold layer (which is the complementary form of the 2D structure), and finally z=125 nm corresponds to top of the upper plane of the structure (also top of the overall structure).

Resulting field maps show hot spots and cold spots, which are more evident on x-z and y-z planes. When comparing two plasmonic structures it is evident that the 3D structure provides electric field intensity enhancement in the overall volume with maximum 7.2-fold enhancement factor compared to the field enhancement of 2D structure. Note that the enhancement of 2D structure occurs only around the sides of the square, limiting the field enhancement into a small region as expected. Placing emitters having film thicknesses even up to 100 nm will create a difference in the emission intensity of emitters due to Purcell factor enhancement with the increased electric field intensity enhancement in the modal volume density [49].

In order to understand the coupling mechanisms for the 3D checkerboard structure, we divided the structure into two pieces as the upper and lower half gold planes. The upper plane is the remaining structure after removal of the gold plane between z=5 and z=45 nm. Likewise the lower plane is defined as the structure after the gold layer between z=85 nm and z=125 nm is removed. The resulting divided structures are illustrated in Figure 3.3.1 with the unit cell indicated in the inset figure. Figure 3.3.2 can be looked at exactly in the same way with Figure 3.3.2; we placed the upper plane structure instead of the 3D structure and lower plane structure instead of the 2D structure. From the field maps, it is clear that the electric field intensity of the 3D structure is superior to

all of the structures. Field enhancement of the 3D structure is a coupled response of the upper and lower planes leading to a larger enhancement than both of them.
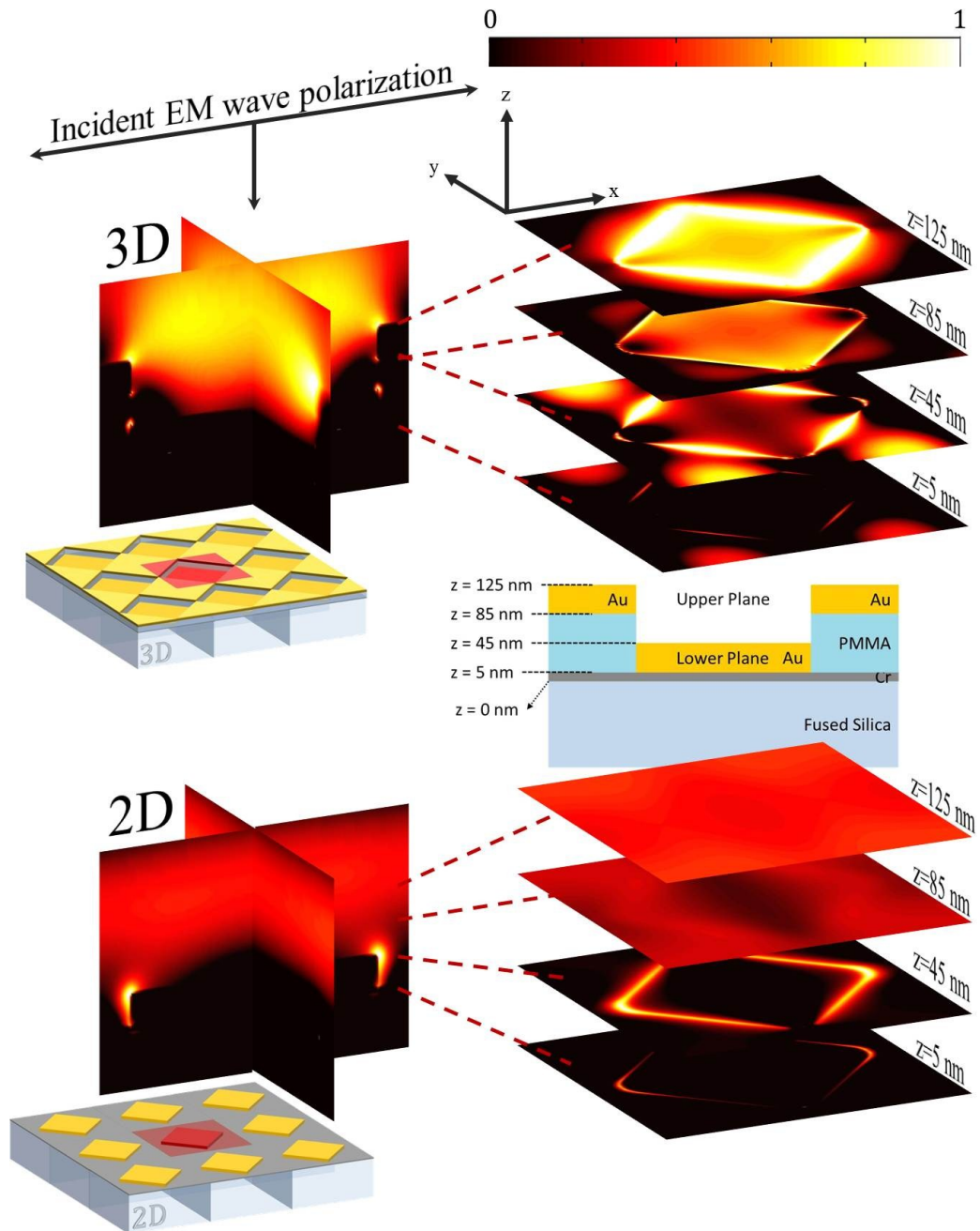
Figure 3.3.1. Spatial electric field intensity distributions for the 2D and 3D structures under 580 nm incident EM radiation. Corresponding z values are shown in the cross-sectional view in the middle.
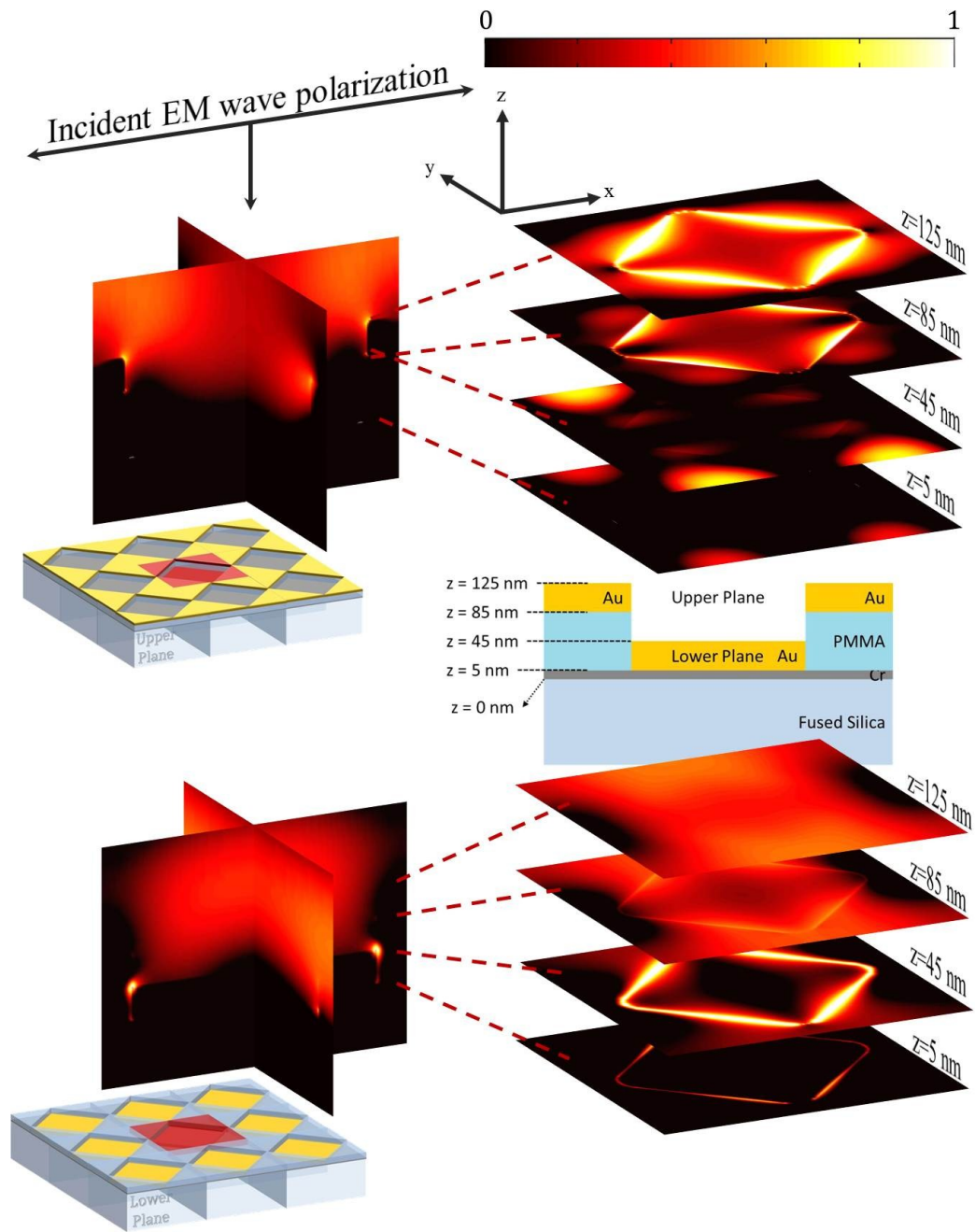
Figure 3.3.2. Spatial electric field intensity distributions for the upper half plane and lower half plane of the 3D structure under 580 nm incident EM radiation. Corresponding z values are shown in the cross-sectional view in the middle.

To relate the observed nearfield electric field intensity maps to the farfield response, which we can measure, we compared absorptance curves of the 2D and 3D structures with the upper and lower plane structures in Figure 3.3.3. As we can see the main resonance peak in the 3D structure is originated from the upper plane response. However, the blueshift observed between these structures implies coupling between the upper plane and lower plane in the 3D checkerboard structure.

In order to observe the response to effective medium change of the 2D and 3D checkerboards, we placed aluminum oxide layer conformally covering the structure. Conformal coating is suitable for atomic layer deposition coating, which we investigated in our experiments. Changing the aluminum oxide layer film thickness from 10 to 25 nm with 5 nm steps, we obtained a redshift in the 3D checkerboard (Figure 3.3.4) but no change in the resonance frequency of the 2D structure (Figure 3.3.5). Increase in the bulk resonance around 450 - 500 nm in both structures can be explained with the guiding mode effect of Al_2O_3 layer. This effect is more obvious from our bulk gold film coating of Al_2O_3 simulations and experiments carried out in metal enhanced fluorescence study in Figure 5.1. Trapping the incident light increases the absorptance, which is effective over the entire spectrum of the 2D structure.

Another interesting observation is that lower plane structure shows higher absorptance than 2D structure, although they have similar structures except for the PMMA pillars in the lower plane structure. The peak around 715 nm is also present in the 2D structure as the case of 0 nm thick Al_2O_3. However, it is quite weak and gets stronger as we increase the alumina thickness. This effect can be explained by the grating counterpart of the 3D checkerboard structure. 3D-like grating structure is shown on the top of Figure 3.3.6 with important dimensions. As it can be seen from Figure 3.3.7 two resonances observed at 580 nm and 715 nm in the 3D-like grating structure are the two modes of 3D structure and 2D

structure, respectively. From Figure 3.3.6 we observe that the resonances both at 580 and 715 nm exhibit the coupling behavior between the upper and lower plane, whereas resonance at 715 nm occurs stronger than resonance at 580 nm. This observation proves that the 3D structure enhances the resonance mode at 580 nm. It is also the case for the 2D structure and the lower plane structure.
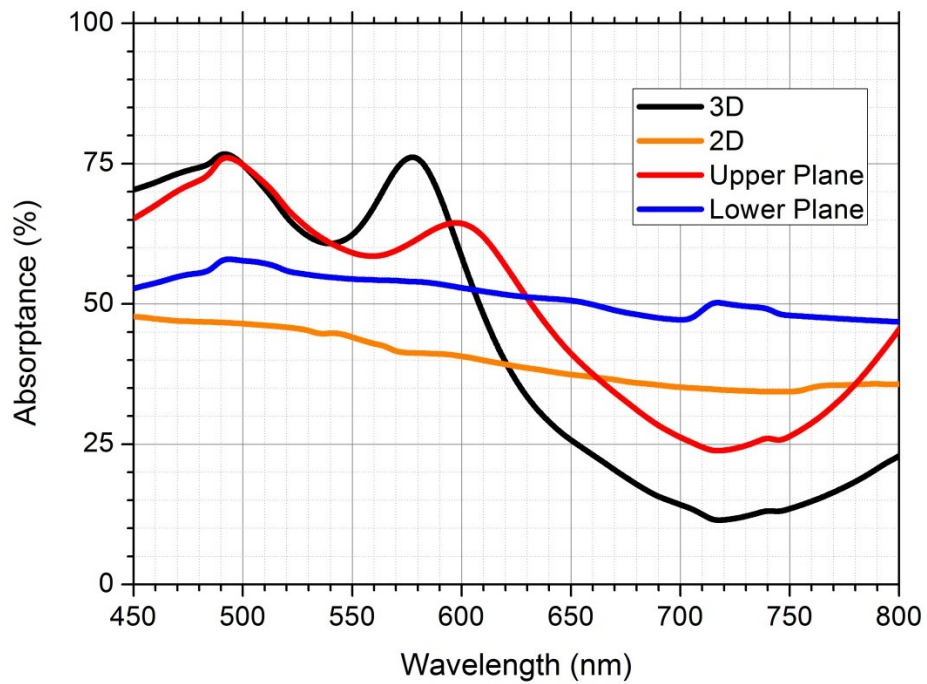
Figure 3.3.3. Comparison of the 3D structures with its two planar components labeled as the upper and lower planes shown in Figure 3.3.2. The 2D structure is also shown for comparison.

As we stated earlier, one of the advantages of the checkerboard structure is its two-fold symmetry. As we observed from Figure 3.3.7, the 3D-like grating structure shows quite strong resonance in the TM illumination case, however, it shows almost no resonance under the TE illumination since surface plasmon polaritons cannot be excited with TE excitations. If we take their average response as the unpolarized light response as shown in Figure 3.3.7, the strength of the 3D checkerboard structure is more evident since its response will be the same for all illumination types under normal incidence.
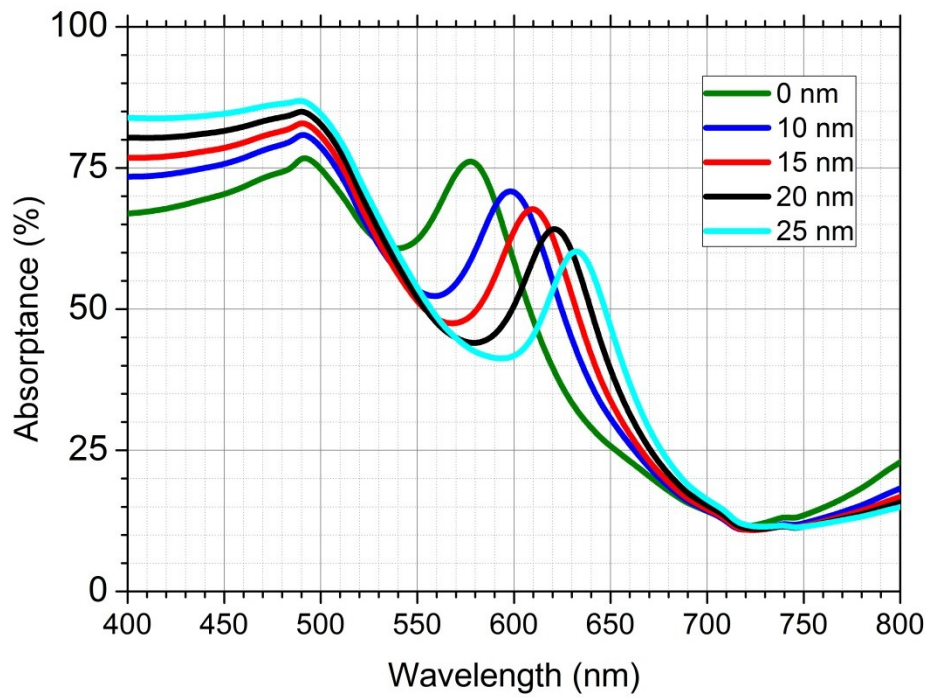
Figure 3.3.4. Simulated absorptance of the 3D structures with varying aluminum oxide thickness.
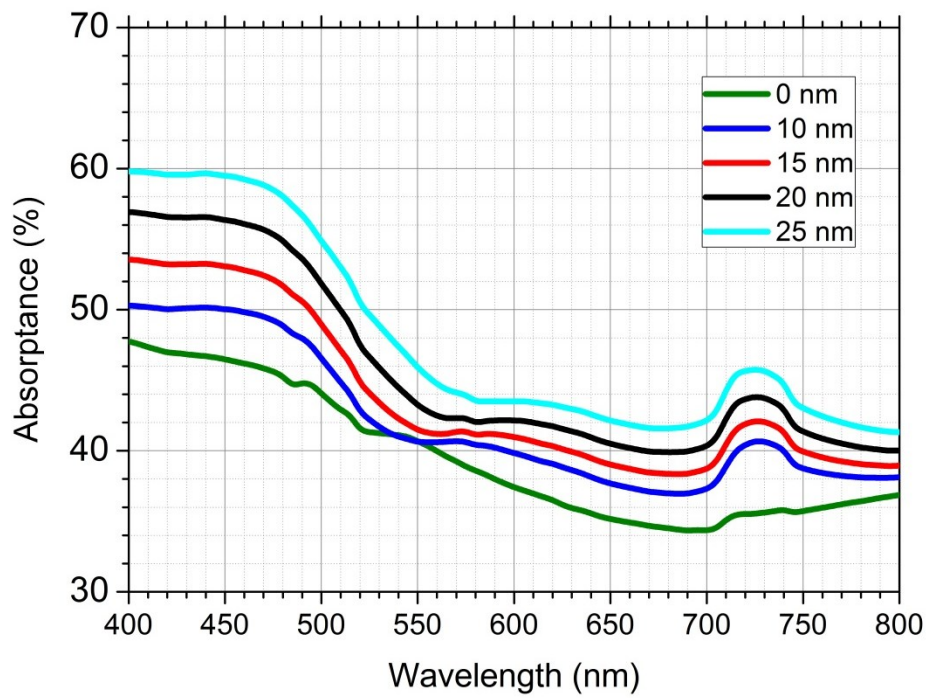
Figure 3.3.5. Simulated absorptance of the 2D structures with varying aluminum oxide thickness.
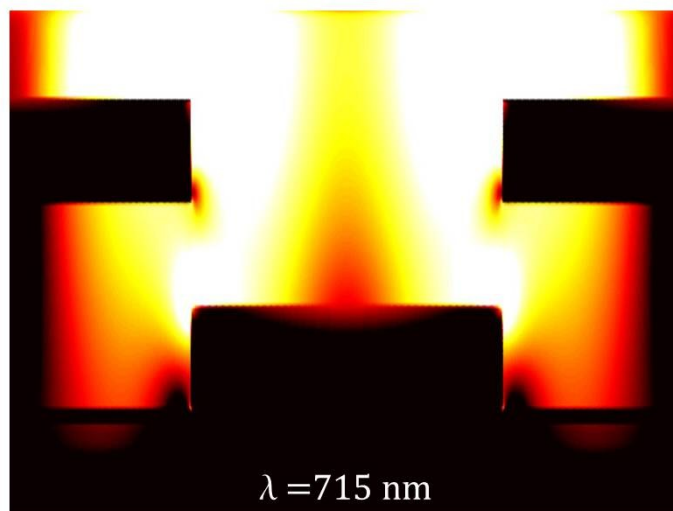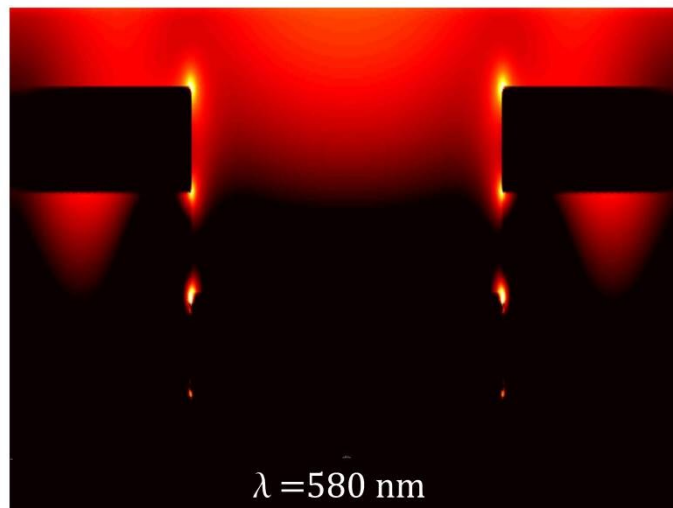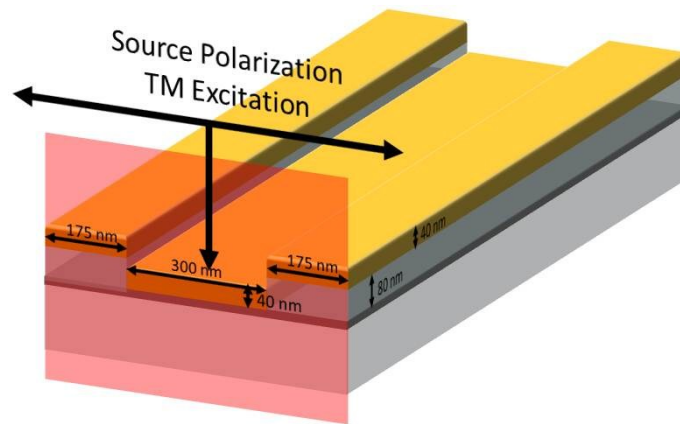
Figure 3.3.6. Illustation of the 3D-like grating with 350 nm periodicity and TM excitation polarization direction of the source (top). Electric field intensity maps at the two resonant wavelengths observed in Figure 3.3.7 (bottom). Color scale is in the logarithmic scale and the same in the Figure 3.3.1 and Figure 3.3.2.

27
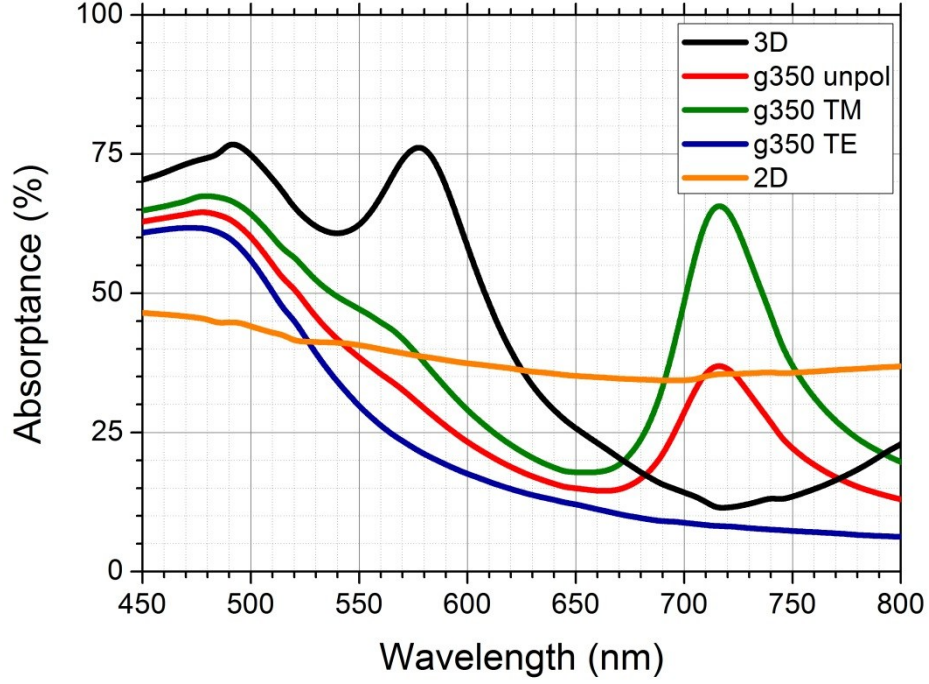
Figure 3.3.7. Percent absorptance of the 2D and 3D checkerboard structure compared with the grating having similar periodicity properties as the 3D checkerboard.

Taking the upper plane and lower plane responses as two complementary shapes, we can apply volume plasmon sum rule to the surface plasmon resonances as

$$1/\lambda_u^2 + 1/\lambda_p^2 = 1/\lambda_{sp}^2 \tag{8}$$

where $\lambda_u = 600$ nm is the resonance wavelength of the upper plane structure, $\lambda_l = 720$ nm is the resonance wavelength of the lower plane structure, and λ_{sp} is the surface plasmon resonance wavelength of the gold, which is redshifted due to interband contributions modeled as the Lorentzian lineshape with a central wavelength at 450 nm from Ref. [37]. Our calculation gives $\lambda_{sp} =$

461 nm, which is quite close to the value from the literature. Also note that bulk contributions observed in the simulations are redshifted with respect to 450 nm.

To compare the simulation results for the 3D checkerboard with the experiment, we calculated the quality factor of the resonance using Equation (6). Quality factor is also related to the oscillation strength of the resonance. To calculate the plasmonic response originated from the structural effects, we fitted two Lorentzian lineshape functions to the absorptance curve of the 3D checkerboard structure as shown in Figure 3.3.8. The quality factor of the plasmonic structure resonance is found to be 8.92. Note that the bulk resonance fit does not seem to be correct due to some simulation where the periodicity of the simulation region is close to the bulk resonance peak.
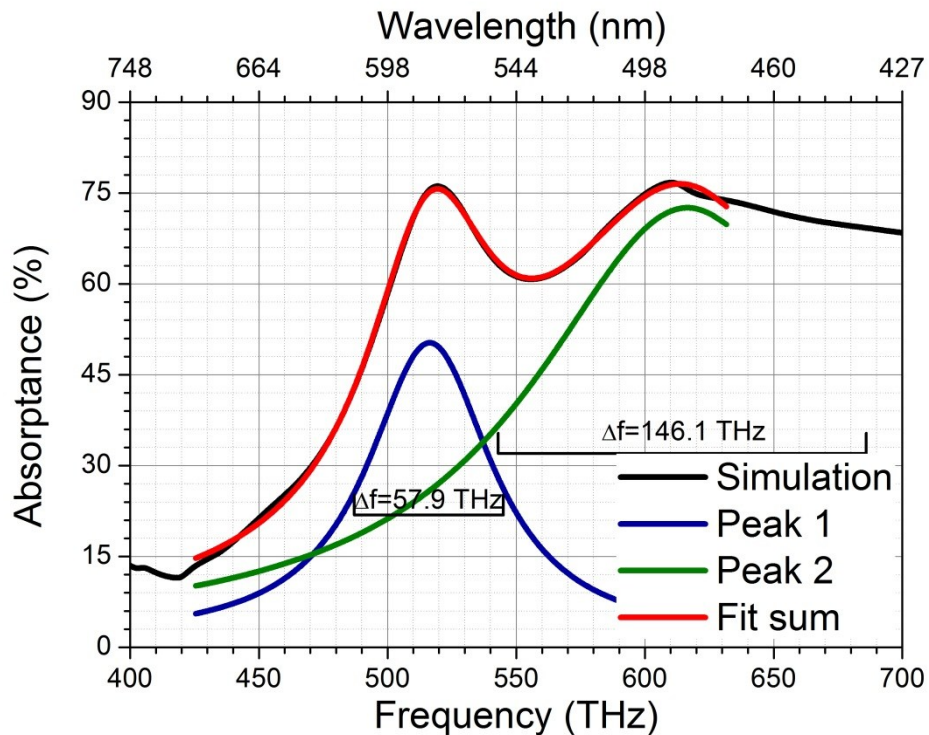
Figure 3.3.8. Percent absorptance data for the 3D checkerboard structure obtained from simulations and two fitted Lorentzian lineshape functions. Peak 1 corresponds to the checkerboard structure plasmonic response and Peak 2 is due to the bulk response of gold.

29

Chapter 4

Experimental Study

Following our theoretical study using FDTD simulations, we fabricated our checkerboard structure design using electron beam lithography (EBL) technique. EBL step is optimized in terms of the exposure dosage of the bilayer PMMA resist, and developer and stopper durations. Fabrications are optimized iteratively using characterization methods. We can classify the characterization methods into two main groups as the structural and optical characterizations.

Structural characterization starts with the determination of metal coating thickness and surface roughness, which are measured using ellipsometry and atomic force microscopy, respectively. Each fabrication is followed by scanning electron microscopy (SEM). If SEM results satisfy the structure sizes, atomic force microscopy is used to determine the pit depth of the 3D structure and double-check the gold thickness for 2D structure.

Optical characterization methods include brightfield optical microscopy in reflection and transmission configurations. Confocal microscopy and time-resolved fluorescence methods are also used to observe photoluminescence enhancement of quantum dots.

4.1 Fabrication Methods

4.1.1 Electron Beam Lithography

In electron beam lithography (e-beam lithography or EBL) technique, an electron beam scans the surface at nanometer scale sensitivity using quite sensitive vector based controller. Although there are dedicated EBL systems operating at 100 kV acceleration voltages, it is quite common that integration of qualified scanning electron microscope with a lithography controller, which is the case for our setup.

As positive tone lithography resist, we used bilayer with PMMA 495 K and 950 K having A2 concentration after spin coating and baking on hot plate. It is critical to prevent the charging effects during EBL. Indium tin oxide (ITO) is a commonly used transparent conductor for EBL charge neutralizer. However, sputtering it requires extra effort to achieve smooth ITO films on fused silica. Instead, it is possible to use a thin chromium layer, which is also transparent and known as the adhesion promoter for gold-silica interface.

While performing EBL step, it is important to perfectly focus the e-beam on the sample before exposure starts. Any astigmatism effect will distort the desired structure as shown in Figure 4.1.1.1.a. It is worth mentioning that there is a theoretical limit for minimum linewidth that can be achieved by EBL, which is limited with the e-beam spot. For our EBL system, having 0.8 nm imaging resolution does not necessarily mean patterned feature sizes can be made down to 0.8 nm resolution. Secondary electrons reflected from the surface expose the resist additionally in all directions, smoothing the desired sharp features. This effect is called proximity effect and sometimes can be the main limit on the achievable minimum feature size. High accelerating voltages and small spot sizes can reduce the proximity effect but never completely overcome it.
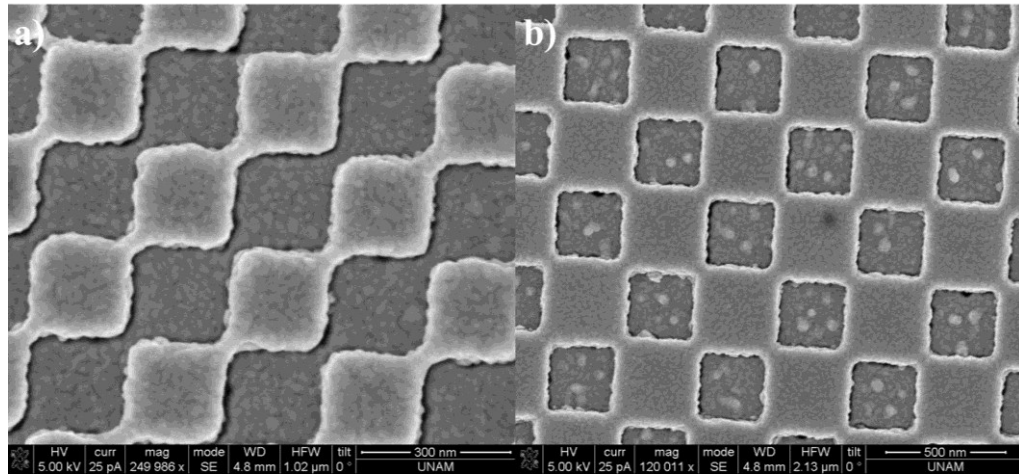
Figure 4.1.1.1. a) EBL performed using scanning e-beam with astigmatism. b) Underdeveloped resist without applied oxygen plasma cleaning step.

Depending on the PMMA thickness, applied exposure dose should be optimized. For this purpose, a desired structure is patterned in small overall sizes with dose matrices. Dose matrices are created by changing the exposure dose by small steps. After controlled developing time in developer solution, a trial sample is observed under scanning electron microscope and the optimum structure can be determined by the observation. Optimization again must consider the required time to pattern the resist since increasing dosage level means linearly increased exposure times. In order to decrease this duration, the spot size can be increased in the expense of reduced resolution.

Finally, exposed PMMA resist is developed in the developer solution. Generally developing times are within 30 - 60 s range with 1 min stopper solution duration. However, for thin samples, shorter develop times can be sufficient. While overdeveloping rounds the corners and changes the feature sizes significantly, underdeveloping can create residues (Figure 4.1.1.1.b) in the exposed areas, which can cause several problems during liftoff step and even can result in no liftoff.

4.1.2 Thermal Deposition Technique

Thermal deposition, or thermal evaporation technique, depends on the deposition of evaporated material (generally but not necessarily metal) on a substrate under high vacuum (~5 µTorr). The material that will be coated is placed in a boat generally made of tungsten or molybdenum and a high current (typically around 100 A) is passed through the boat. Then, heated material starts to evaporate due to low vapor pressure facilitated by high vacuum conditions. At the same time deposition mass thickness is monitored by a detector calibrated using correction factor called tooling factor.

In thermal deposition technique, the most important parameter to be optimized for desired fabrication and surface roughness subject to application is the deposition rate. Low deposition rate, together with rotating the sample, ensures the surface uniformity; however, this creates isolated nanoislands when the adsorption to the substrate is weak. This problem can be overcame using different deposition rates like 0.1 nm/s at the beginning, then followed by 0.04 nm/s rate, which gives good results for gold deposition on fused silica and PMMA substrates. Vacuum level, substrate distance from the source and substrate temperature are additional parameters; however, our system does not allow us to modify these conditions.

4.1.3 Sample preparation: Atomic Layer Deposition

We used atomic layer deposition (ALD) technique to coat Al_2O_3 conformally to create spacing level between QDs and metallic plasmonic structure in order to prevent quenching effects and fully exploit the electric-field enhancement. We coated Al_2O_3 at 150 °C, although higher temperature coatings could give better results, since our 3D structure consists of PMMA and gold boundaries, which are vulnerable to high temperatures. The relation between ALD cycles and deposited oxide thickness is given in Figure 4.1.3.1. The results indicate that

33

there is quite linear relation between the cycles and the oxide thicknesses as expected. Using these data, we commonly took 10 cycles to make about 1 nm Al_2O_3 in our experiments.
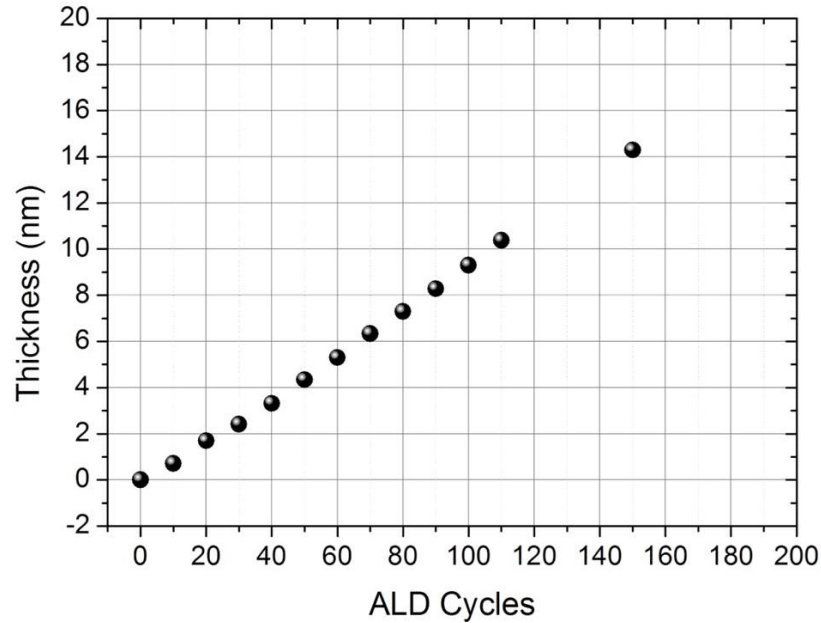
Figure 4.1.3.1. ALD cycles and its corresponding layer thickness for Al_2O_3. The relation reads that 10 cycles $\cong$ 1 nm Al_2O_3.

4.2 Fabrication Steps and Parameters

350 μm thick double side polished fused silicon oxide wafers are prepared as 2x2 cm^2 substrates. In order to prevent charging effects on the silicon oxide substrates during electron beam lithography (EBL) and imaging with scanning electron microscopy, 3.5 nm thick chromium is deposited at a rate of 0.03 nm/s onto the substrates using electron beam deposition (EBD) technique. Then, to promote lift-off process for 2D structure and also prevent sidewall formation for 3D structure, we coated bilayer PMMA as the EBL resist. After 5 min prebake on hotplate at 180 °C, PMMA 495 K with A2 concentration is spun at 5000 rpm rate for 45 s. Immediately, 90 s postbake is applied and the second layer is coated with PMMA 950 K, which has a higher molecular mass compared to the

34

A2 concentration again at 5000 rpm for 45 s as shown in Figure 4.2.1.a. Finally, 10 min postbake is applied to provide a smooth PMMA surface.

After substrate preparation, the most critical process of the structure fabrication is EBL (Figure 4.2.1.b). It is also the bottleneck of the fabrication in terms of parallel processing. All the other steps can be performed in parallel; however EBL should be processed on the samples one by one with extreme care after optimization. During EBL process, we used Nova NanoSEM 600 from FEI integrated with ElphyPlus from Raith as a lithography controller. To define the sharp corners of the checkerboard, we reduced the electron beam current to 13 pA, which will reduce the radius of the electron beam onto the resist. Also, usage of the highest possible voltage as 30 kV prevents the backscatter of the electrons with an increased spot size. During the calculation of the e-beam dosage values, the measured current 32 pA is used. Optimum area dosage is turned out to be 300 $\mu C/cm^2$ after several trials with dose matrices. For photoluminescence measurements with confocal microscopy we fabricated 49x49 μm^2 structures as the write field area of the software limits us to 50x50 μm^2 and for time-resolved fluorescence measurements we made 10x10 matrix of the single 49x49 μm^2 structure. Whole lithography process takes slightly more than 8 hours. After e-beam scanning, to define the patterns, PMMA developed in a mixture of methyl isobutyl ketone (MIBK) and isopropanol alcohol (IPA) with 1:3 ratio from MicroChem Corp. for 13 s and then rinsed in extra pure IPA solution for 20 s. Developing process is followed by additional O_2 plasma etching step, which is applied for 30 s using Asher system from Nanoplas in order to remove the residuals of PMMA during developing (Figure 4.2.1.c). Asher is another critical step for the liftoff process during the 2D checkerboard structure fabrication.

Patterned PMMA samples are coated with 40 nm thick gold using thermal deposition system. During deposition, in order to facilitate adhesion of gold on PMMA (for the 3D structure upper plane) and on chromium (both for the 2D

structure and lower plane of 3D structure) first 15 nm thick gold are coated relatively fast at a rate of 0.07 nm/s and, for the remaining 25 nm, a smooth surface is attained by coating gold at a rate of 0.04 nm/s. the 3D checkerboard structure fabrication finishes at this step, and for the 2D structure, an additional liftoff process is applied.

Liftoff is the latest and most important step for the 2D structure fabrication. Acetone is the general solvent for PMMA; however it leaves residues on the surface. In the literature, 1,2-dichloroethane is shown to be a better solvent for PMMA [50]. In our first trials, we observed adhesion of the removed parts on the samples. Placing the sample upside-down solves this adhesion problem. After keeping the sample for 2 hours in the solvent, instant dipping into ultrasonic bath gives quite good liftoff results.

In order to study and control metal enhanced fluorescence effects on our structure, aluminum oxide (Al_2O_3) is coated with atomic scale control using atomic layer deposition system Savannah from Cambridge Inc. Since the 3D structure involves gold-PMMA interface, a high temperature processes can damage the sample. We thus deposited Al_2O_3 at 150 °C (almost lowest temperature edge of the ALD window) [51]. Subsequently, giant QD solution in toluene is spin-coated at 3000 rpm for 3 min in order to ensure that the toluene is evaporated completely.
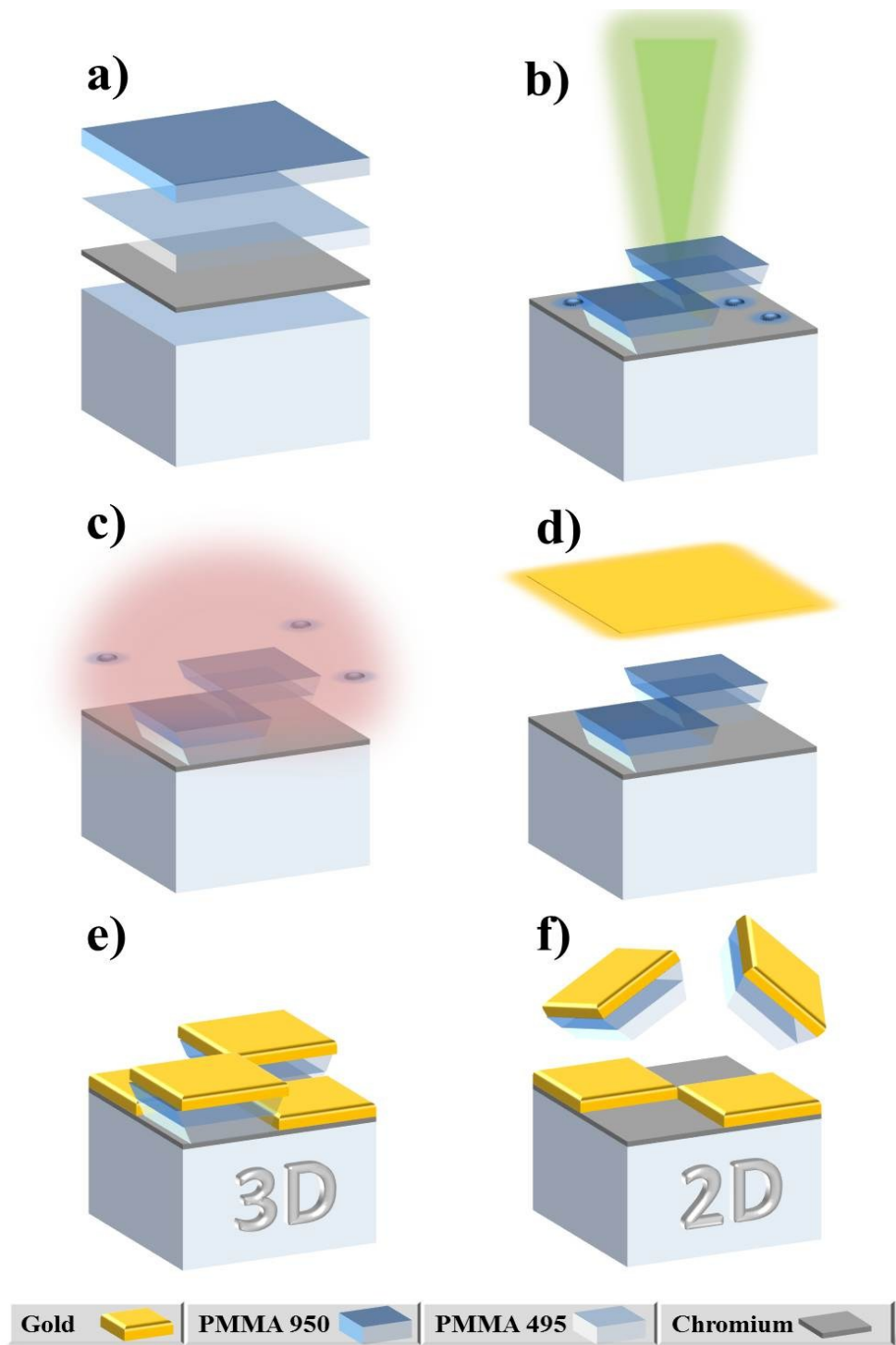
Figure 4.2.1. Process flow is shown step by step: a) On pre-deposited 3.5 nm chromium, PMMA 495 K and PMMA 950 K are spin-coated. b) Electron beam scans the pattern on PMMA resist. c) O₂ plasma cleaning removes the PMMA residues after developing. d) 40 nm thick gold is thermally evaporated. e) 3D structure fabrication is completed and f) an additional liftoff step is required for 2D structure.

4.3 Characterization Methods

Characterization of the fabricated structures is performed under two main aspects, which can be classified as the structural and optical methods.

4.3.1 Structural Characterization

Structural methods consist of scanning electron microscopy (SEM) and atomic force microscopy (AFM). While SEM is being faster than AFM for observing planar features including their sizes, it lacks the capability to measure the vertical features like pit depth size for 3D checkerboard structure and gold thickness measurement for 2D structure. AFM is not as fast as SEM; however it is capable of mapping surface roughness at nanometer scale sensitivity and precisely measuring the vertical features. We generally used AFM for pit depth measurements and thermal evaporation tooling factor correction.

4.3.1.1 Scanning Electron Microscopy

Scanning electron microscopy is a surface imaging technique with subnanometer resolution. A highly focused electron beam scans the surface using magnetic lenses and a detector collects the scattered electrons from the surface. These collected electrons can be either backscattered electrons or secondary electrons depending on the position of the detector. In our measurements, we used secondary electrons with built-in TLD detector in our electron beam lithography system Nova NanoSEM 600 from FEI. In SEM measurements, there are several main parameters to obtain a good image like accelerating voltage, emission current (or spot size) and working distance. High accelerating voltages mean more energetic electrons at shorter wavelengths providing a better resolution at the expense of a lower contrast and structure damage. Similarly, increasing the spot size gives a better contrast; however, more electrons hitting the surface leads to more heating of the surface, giving

rise to surface deformation again. Finally, when the working distance is small so that the sample is close to the electron gun, we obtain tight focusing of the electron beam with a high resolution but a reduced intensity and thus decreased contrast. In order not to damage the sample, we do not use 30 kV accelerating voltage as we use during the fabrication. Instead 15 kV acceleration voltage with 44 pA current is used during the structure imaging at 5 mm working distance.

4.3.1.2 Atomic Force Microscopy

Atomic force microscopy measurements are performed with WITec alpha300 S in AC tapping mode with a tip having a natural resonance around 280 kHz. In AFM measurements, PID gain coefficients and driving voltage should be optimized in order to obtain good surface topography image. We use 0.65 V driving voltage during our measurements.

4.3.2 Optical Characterization

Optical characterization is the most challenging part for EBL fabricated small samples with micrometer sized features. In order to collect the reflected and transmitted signal only from our 50 x 50 μm^2 sized structures, we used optical microscopes for collecting light and obtaining spectral response information in brightfield configuration. Confocal microscopy is used to obtain photoluminescence of QD films on our structure with μm sensitivity. Finally time-resolved fluorescence measurements are performed to obtain the decaying lifetimes of QD films and comparing the intensities accordingly.

4.3.2.1 Brightfield Optical Microscopy

Brightfield optical microscopy measurements are obtained using two different microscopes due to their illumination and collection geometry. Transmittance measurements are made using Nikon Ti-U Eclipse inverted microscope with

40X objective. Reflectance measurements are performed using Probe System from Cascade Microtech with 20X objective. Spectral data is taken using Maya 2000 spectrometer from Ocean Optics fiber coupled to the outgoing ports of the microscopes. Since our fabricated structures are limited in the overall size to 50 μm, in order to ensure that collected light is only coming from the structure we used an adjustable aperture iris being capable of full closure. Using a regular CCD camera we observed the image of the structure under illumination and ensured no light was coming from outside.
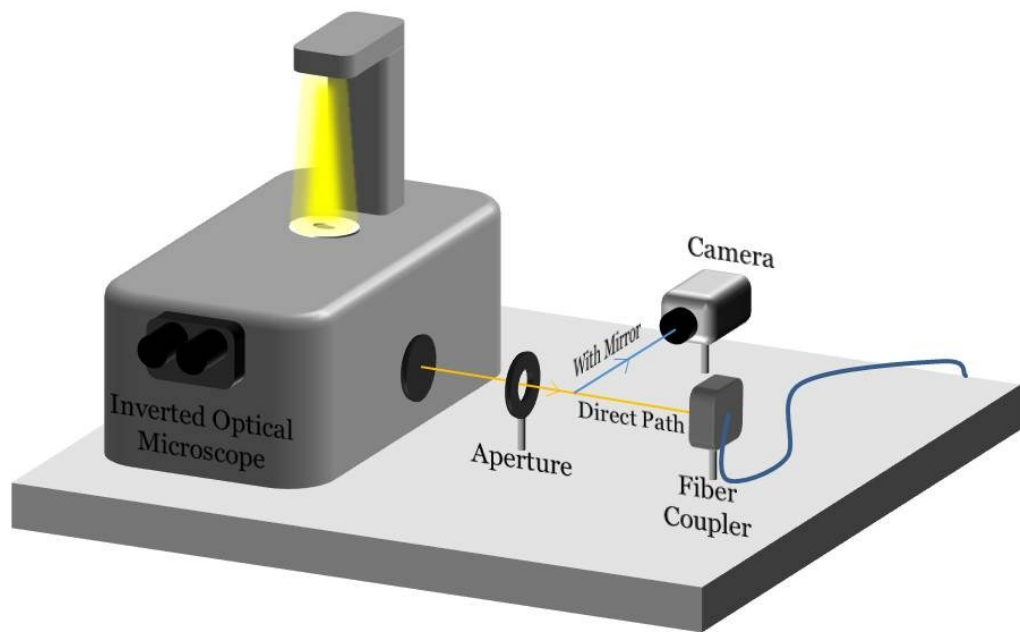
Figure 4.3.2.1.1. Optical setup schematics for transmission and scattering spectra measurements using inverted optical mocroscope. We used a flip mirror mount the guide the optical path for structure selection and spectrum acquisition.

A legitimate way of taking this kind of measurements is to build 4f system using two lenses by placing aperture on the first image and fiber coupler (and CCD) on the second image plane. However, we observed a high signal drop with increasing number of optical components and compared the results with the system shown in Figure 4.3.2.1.1. Since placing an aperture at another position

than the image plane only distorts spatial profile of the signal, we did not lose any data and we used the configuration in Figure 4.3.2.1.1 in all experiments. Note that we used a flip mounted mirror to switch the incoming beam to the camera to image the sample or to the spectrometer with a fiber coupler to obtain spectral data.

Since we work in the frequency domain, it is easy to deconvolve the system response by simply dividing obtained signal ($I_m(f)$) to the system response ($I_s(f)$) as

$$I(f) = I_m(f)/I_s(f). \qquad (9)$$

In the reflectance measurements we also used a backside polished protected silver mirror from ThorLabs Inc. to normalize the data. During this normalization process it is also important to consider the mirror response obtained from the vendor.

4.3.2.2 Confocal Microscopy

Confocal microscopy is the commonly used technique for fluorescence imaging. Excitation light (preferably but not necessarily a laser source) is sent to the sample using an objective and then through the same objective from the same optical path light, it is collected using a spectrometer. In order to reject the out-of-focus light coming to the spectrometer, an aperture is placed in front of the spectrometer. As a result, depending on the size of the laser beam waist size on the imaging plane within the sample, confocal microscopy can have a submicron resolution. Measurements in this study are obtained using WITec alpha300 S integrated with a solid state laser operating at 532 nm wavelength. A 100 x 100 μm^2 area is tracked with 1 μm precision with a laser beam waist no larger than 2 μm. Laser power is kept constant for fair comparison between the 2D and 3D structures along with the control samples. Also utmost care is shown to keep

laser power low in order not to damage the samples. Since the 3D structure includes PMMA, excess heating can cause structural deformation.

4.3.2.3 Time-Resolved Fluorescence Measurement

Time-resolved single photon counting fluorescence system FluoTime 200 from PicoQuant Inc. is integrated with a photomultiplier tube sensor having 4 ns time resolution and being capable of detecting single photon. QD films are excited with a pulsed solid state laser at 375 nm emission wavelength and with a 200 fs pulse width. Sending laser pulses at 5 MHz repetition rate gives a 200 ns time window for the fluorescence decay curve observation. Exponential fits are calculated using the built-in software FluoFit from PicoQuant Inc. and the reduced chi-squared parameter χ^2 is kept under 0.9, which is the indicator for a good fit quality. In order to take time-resolved fluorescence measurements, we fabricated structures having overall side lengths of 500 μm, which takes more than 10 hours to complete the EBL step.

4.4 Experimental Results

Experimental results are divided into three main parts as the structural characterization results of the fabricated structures to observe that the fabricated structures are the same with the simulated structures. To prove that, SEM and AFM imaging techniques are used. Optical characterization of the plasmonic structures is in the farfield domain and deals with the absorption behavior of the plasmonic structures. We also present the reflectance and transmittance spectroscopy results with respect to the coated aluminum oxide thicknesses. Finally, as an application of the plasmonic structures, we present PL emission enhancement and lifetime control over the QDs using spectroscopic confocal and time-resolved fluorescence measurements.

4.4.1 Structural Characterization of Fabricated Checkerboards

After completing the fabrication of 2D and 3D checkerboard structures, we obtained SEM images as presented in Figure 4.4.1.1. Perspective images are taken with a 35° tilted stage and top view images are obtained in normal incidence. Scalebar is common for both top view images. Bright parts correspond to gold structures in the 2D structure and dark background is due to Cr layer coated on the fused silica wafer. Since the 3D structure is coated with gold everywhere, top view image consists of bright areas compared to 2D image. The measured structure feature size is in good agreement with the simulated structure and rounded corners observed both in the 2D and 3D structures justifies the usage of the rounded corners with 40 nm radius in the simulation setup.

We also checked the sidewall formation for the 3D structure. Cross-sectional image is obtained using focused ion beam (FIB) technique. First, a protective platinum layer is deposited using e-beam with very slow rates to prevent milling during deposition. Then, the second platinum deposition at a high deposition rate using ion beam is performed. The difference between two layers can be observed from Figure 4.4.1.2. Finally, ion milling is performed and a cross-sectional image is obtained on a similar device. Although no sign of sidewall formation is evident from the performing liftoff step for 2D structure, the profile of the cross-section gives additional data to explain the differences between the simulation and the experiment. Bending of the upper layer around the corner is the only observed difference between the simulations and the experiments and can be the reason for the mismatch between the obtained results.

Finally we took AFM images for the pit depth measurement of 3D checkerboard structure, which gave a similar result with the simulation and the film thickness of the gold squares of the 2D structure having 40 nm height proves the thermal deposition tooling factor is correct. Profiles are shown in Figure 4.4.1.3.

2D

500 nm

3D
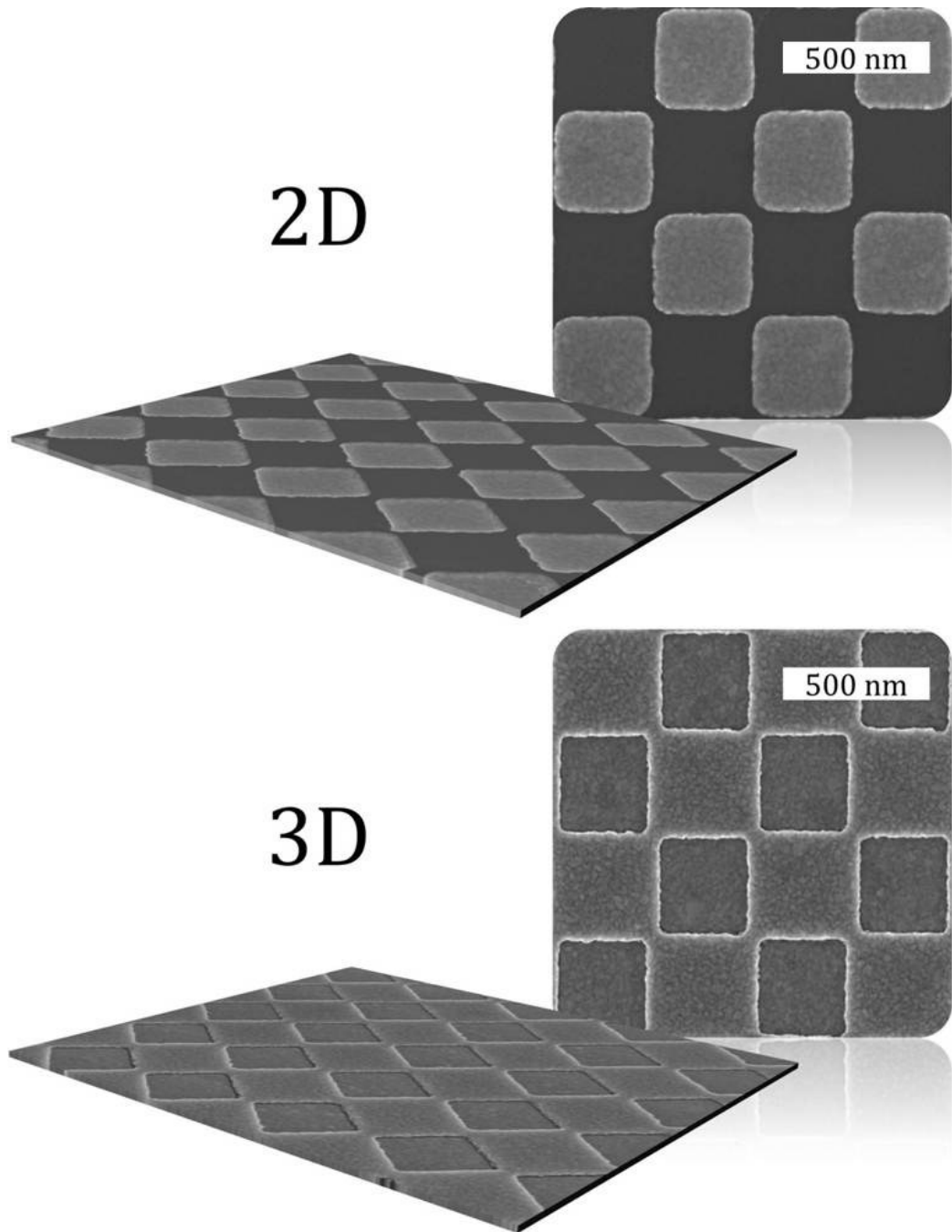
500 nm

Figure 4.4.1.1. Scanning electron microscopy images of the 2D checkerboard from perspective and top views (top) with 3D checkerboard from perspective and top views (bottom). Scalebar corresponds to 500 nm.
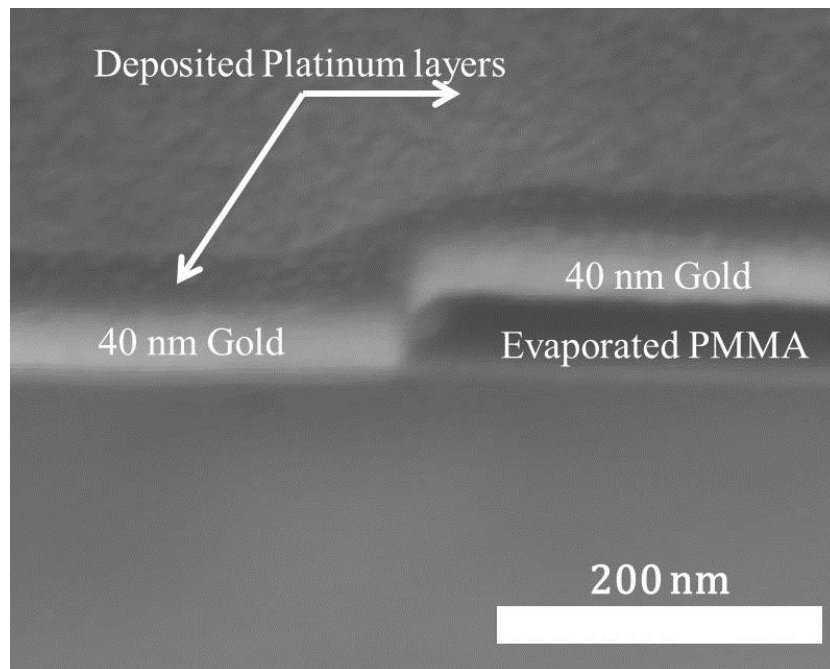
Figure 4.4.1.2. Cross-sectional SEM image of the 3D checkerboard structure.
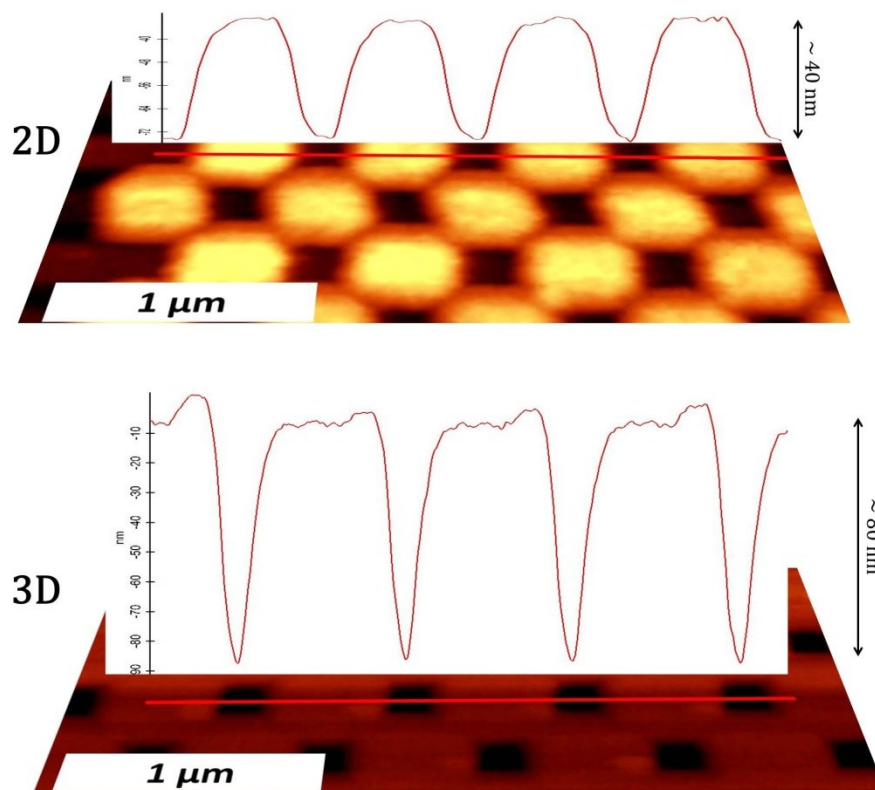
Figure 4.4.1.3. AFM measurements and corresponding cross-sectional topographies indicated with red lines for the 2D and 3D checkerboard structures.

4.4.2 Optical Characterizaiton of Fabricated Checkerboards

After structural characterization verification, we obtained optical characterization results using brightfield optical microscopy in transmission and reflection mode as described in Section 4.3.2.1. Absorptance data is calculated similar to the simulation as the subtraction of reflectance and transmittance data from the unity. The transmittance data for the 2D and 3D checkerboard structures with varying Al_2O_3 thicknesses is presented in Figure 4.4.2.1 and Figure 4.4.2.2 respectively. Similarly, the reflectance data for the 2D and 3D structures are shown in Figure 4.4.2.3 and Figure 4.4.2.4, respectively. From the transmittance and reflectance data, we observe that a thin layer of Al_2O_3 deposition increases the transmittance and decreases the reflectance effectively. Like in the simulation results, this effect can be attributed to light trapping or impedance matching of the plasmonic structure to the air interface. Note that since the duty cycles of the 2D and 3D structures change, their transmittance and reflectance values vary.
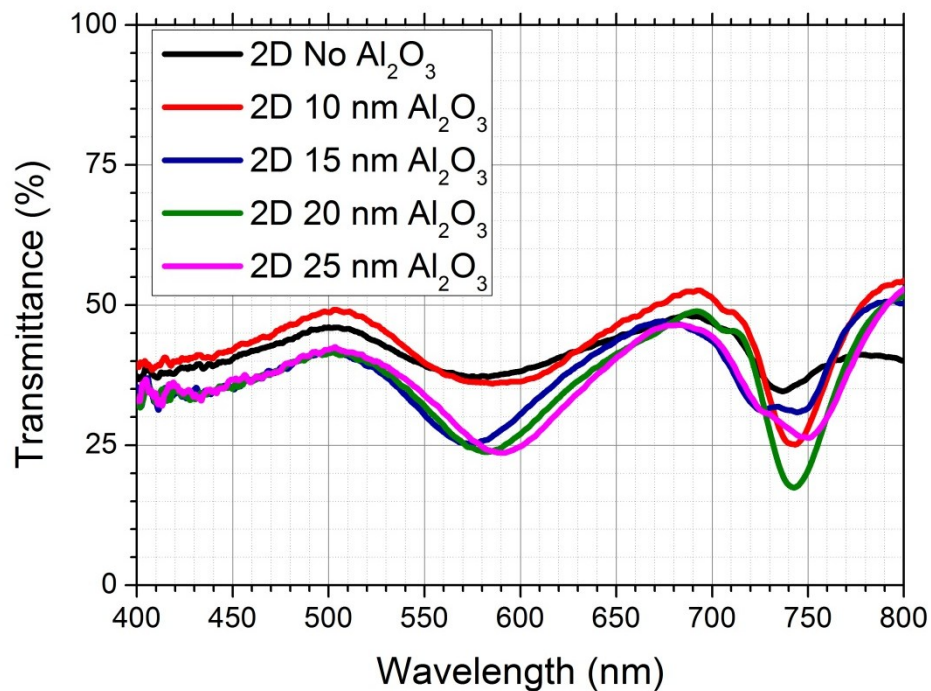
Figure 4.4.2.1. Percent transmittance spectra for the 2D checkerboard structure with different Al_2O_3 thicknesses.
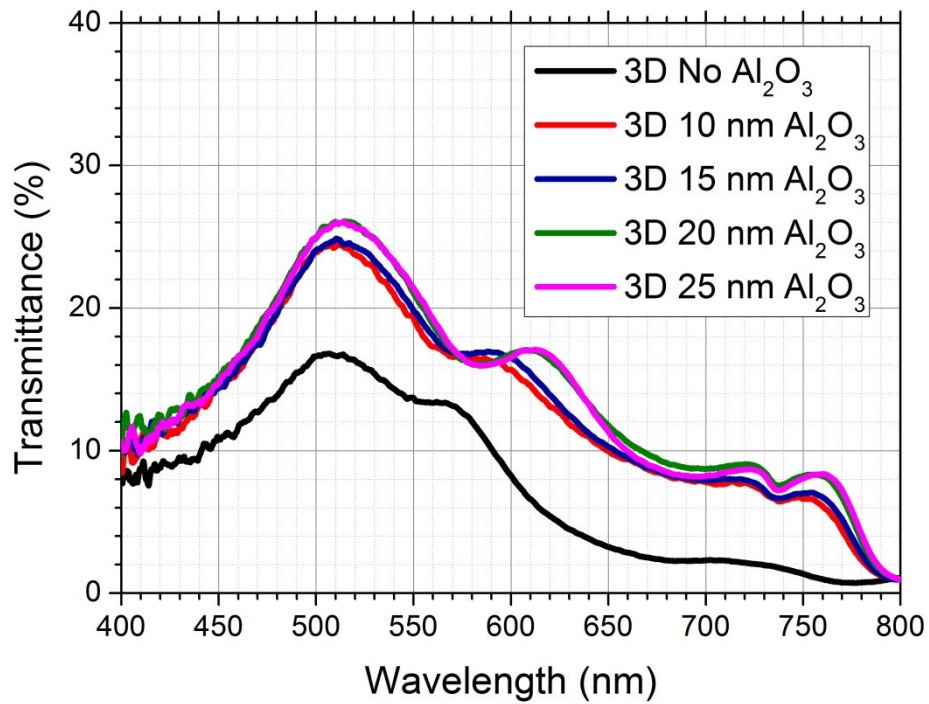
Figure 4.4.2.2. Percent transmittance spectra for the 3D checkerboard structure with different Al$_2$O$_3$ thicknesses
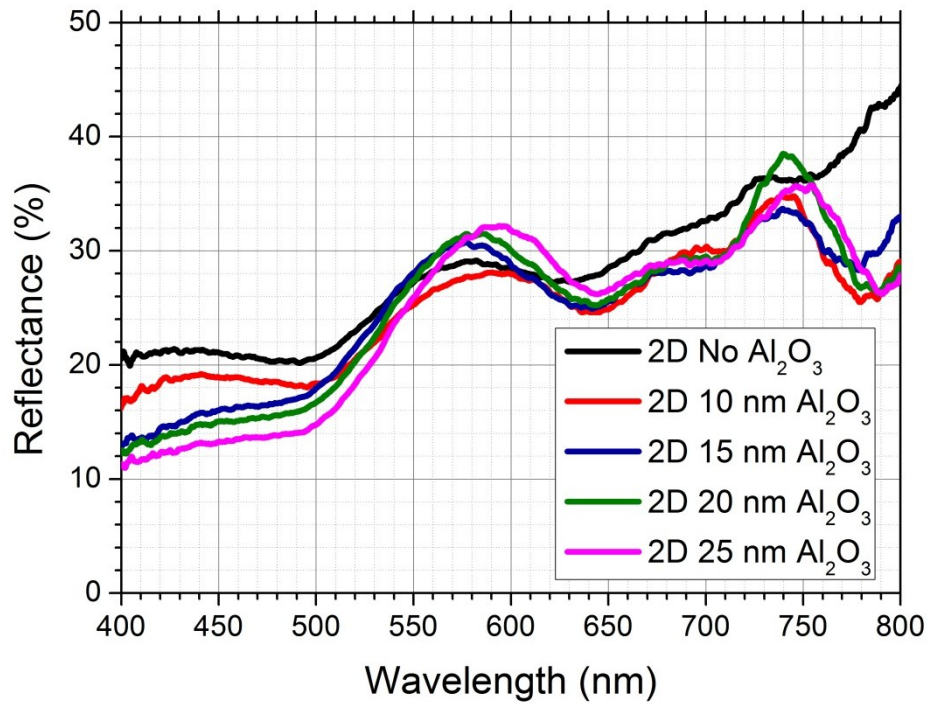
Figure 4.4.2.3. Percent reflectance spectra for the 2D checkerboard structure with different Al$_2$O$_3$ thicknesses.
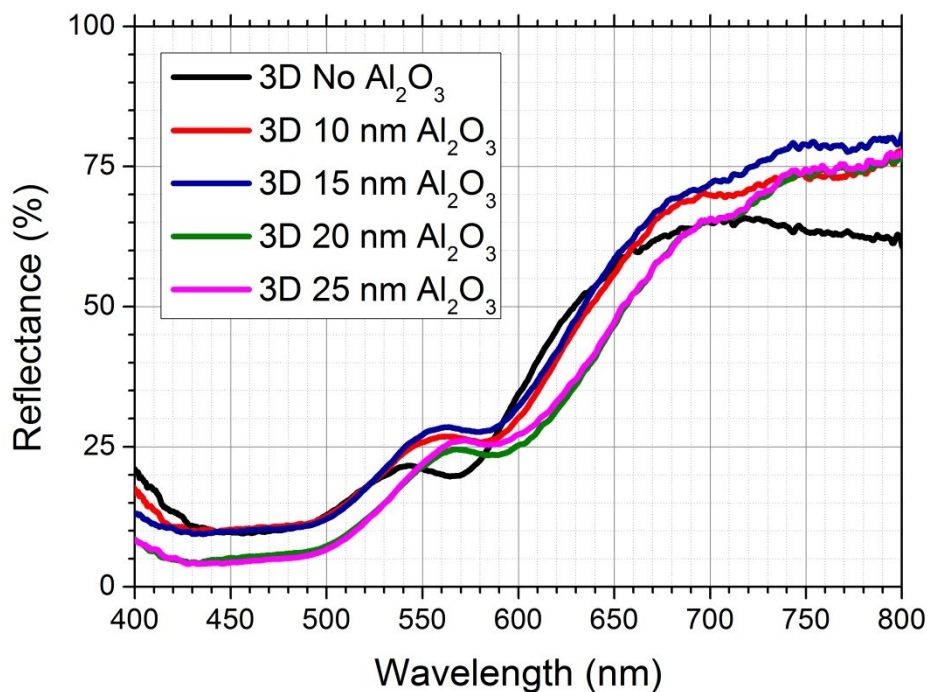
Figure 4.4.2.4. Percent reflectance spectra for the 3D checkerboard structure with different Al$_2$O$_3$ thicknesses.

We observed plasmonic resonance peaks are redshifting very regularly in the simulation with increasing oxide thickness (Figure 3.3.4), however we did not observe these shifts as regular in the experiments. Although we deposited aluminum oxide layers at around the low temperature limit of the ALD window, the deposition time for 100 cycles, corresponding to 10 nm film thickness, was 80 min long which is quite a long time to wait at 150 °C. Certainly, annealing and deformation of the structure occurs. However, from Figure 4.4.2.5 we observe that the structural deformation is not as dramatic as expected. Note that Figure 4.4.2.5 shows the peak absorptance data obtained from Figure 4.4.2.6 for the 3D structure and Figure 4.4.2.7 for the 2D structure. For the 3D structure, increasing the oxide thickness reduces the peak absorptance value at the resonance wavelength, which is redshifted. The 2D structure's peak absorptance values come from the weak peak around the 580 nm wavelength shown in Figure 4.4.2.7. As expected from the simulations, they do not show any

significant redshift behavior and due to the oxide layer effect on the absorptance peak absorptance values slightly increases whereas the peak resonance blueshifts, which can be attributed to annealing effect. The simulated spectral behaviors of both the 3D and 2D structures are quite similar in general trends observed in their experimental data.
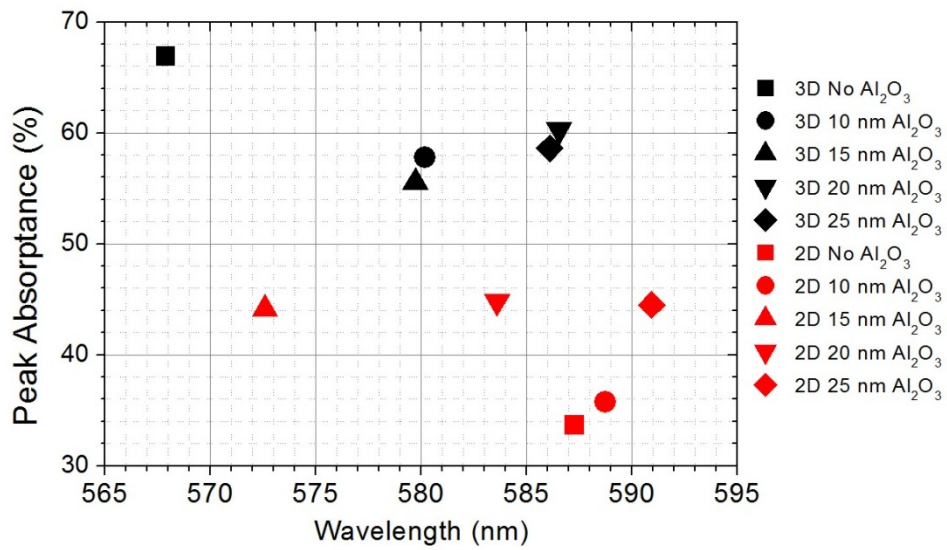
Figure 4.4.2.5. Percent peak absorptance vs. wavelength for different 2D and 3D checkerboard structures with varying aluminum oxide thicknesses.
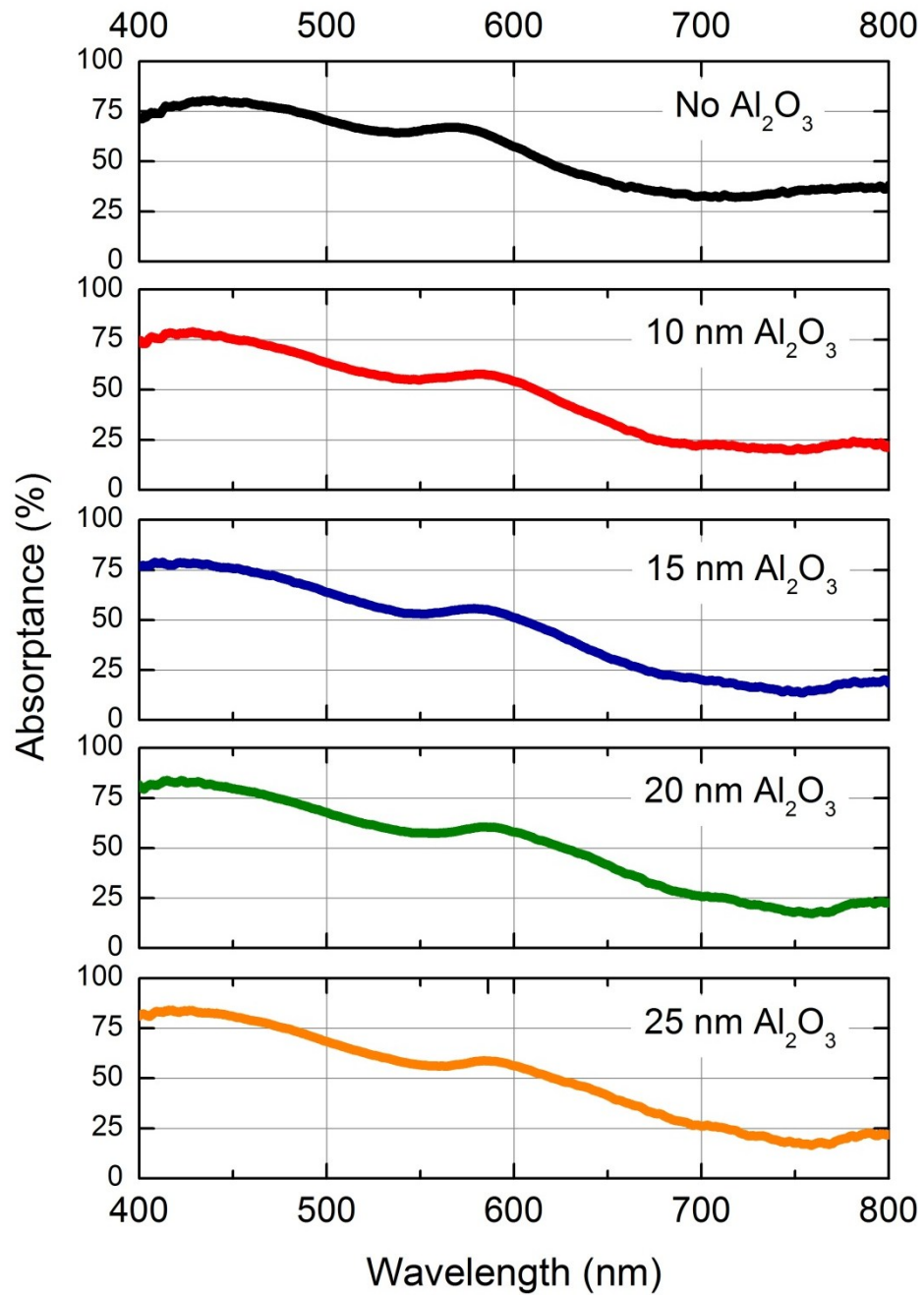
Figure 4.4.2.6. Percent absorptance values for the 3D checkerboard structure with different Al$_2$O$_3$ thicknesses.
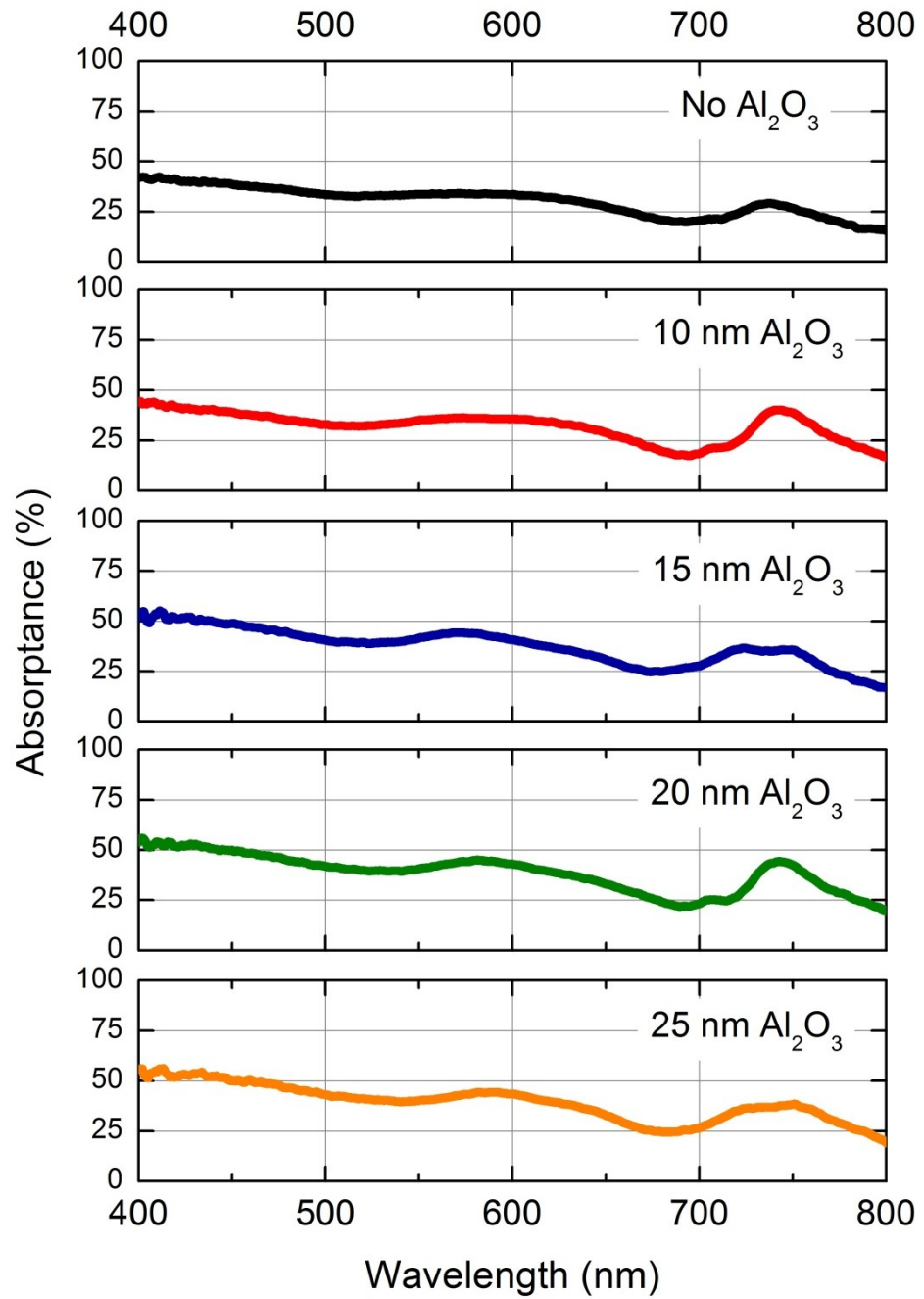
Figure 4.4.2.7. Percent absorptance values for the 2D checkerboard structure with different Al$_2$O$_3$ thicknesses.

We studied the plasmonic behavior of the 3D checkerboard structure from the simulation data by fitting two Lorentzian lineshape functions to separate the bulk response and the structural plasmonic response. We performed the same fitting for the experimental results. In Figure 4.4.2.8, we can see the two resonant peaks. Peak 1 again corresponds to the response of the structure and Peak 2 corresponds to the bulk response of the gold. The plasmonic response of the structure obtained from the simulation and experiment show quite a good agreement as seen from Table 4.4.2.1. Calculated quality factor for the experimental response peak is 7.82, which agrees well with the simulation result of 8.92. Reduction in the quality factor of the resonance can be due to the bending as the corners observed from the cross-sectional image of the 3D checkerboard structure (Figure 4.4.1.2). Note that the resonance wavelength corresponds to 577 nm.
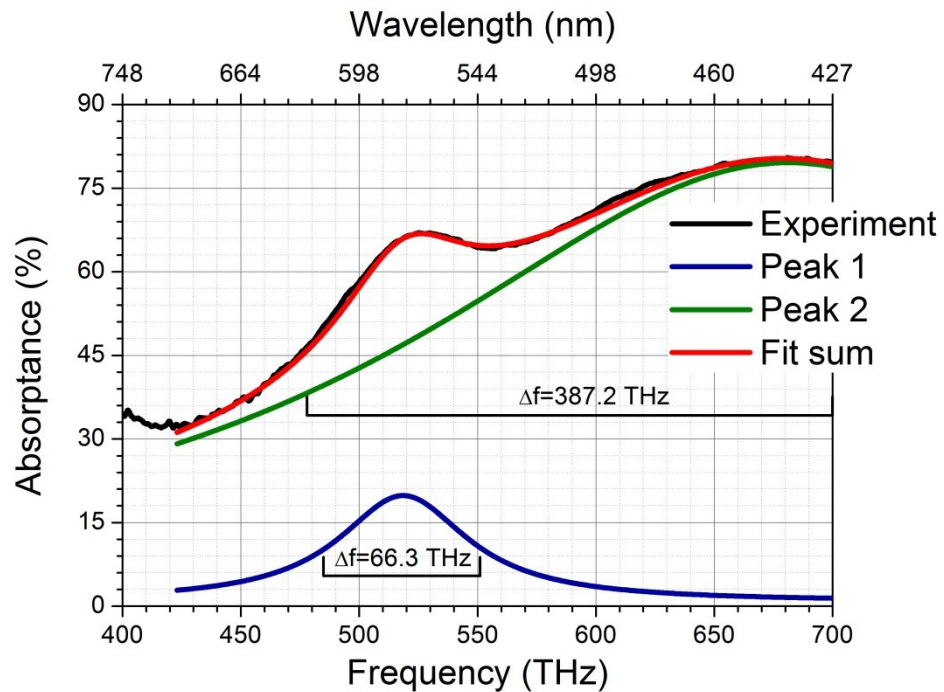
Figure 4.4.2.8. Experimental percent absorptance data for the 3D checkerboard structure and two fitted Lorentzian lineshape functions. Peak 1 corresponds to the checkerboard structure plasmonic response and Peak 2 is due to the bulk response of gold.

52

	Bulk resonance peak center frequency	Bulk resonance peak FWHM	Structure resonance peak center frequency	Structure resonance peak FWHM
Simulation	616.6 THz	146.1 THz	516.4 THz	57.9 THz
Experiment	681.4 THz	387.2 THz	518.6 THz	66.3 THz
Interband contribution model resonance	664.4 THz	143.2 THz	---	---

Table 4.4.2.1. Comparison of Lorentzian fit results of the simulation and experimental data shown in Figure 3.3.8 and Figure 4.4.2.8, respectively. Interband contribution Lorentzian model is taken from Ref. [37]

Chapter 5

Application:

Metal Enhanced Fluorescence and Lifetime Control of Quantum Dots

To study the metal enhanced fluorescence and lifetime control of QDs, we first studied the quenching and enhancement mechanisms in terms of aluminum oxide layer thickness coated on bulk gold films. We deposited aluminum oxide layers using ALD with 1 nm steps on 50 nm thick continuous gold films. Then, we obtained absorptance data of these films and compared them with the simulations as shown in Figure 5.1. Results are in quite good agreement. Subsequently, we spin-coated giant QDs on these films and obtained PL signals. Up to 9 nm, we observe quenching on the metal surface with respect to the control sample of bare fused silica indicated with the red line in Figure 5.2. Note that perfectly continuous smooth gold films should show no surface plasmon resonance effect at the emission wavelength of the giant QDs. However, the enhancement cannot be explained using reflection from the metal since the enhancement value is more than 2 with respect to the fused silica around 25 nm. We can conclude that the resulting gold film is not perfectly smooth and there is definitely coupling between the gold and QDs.
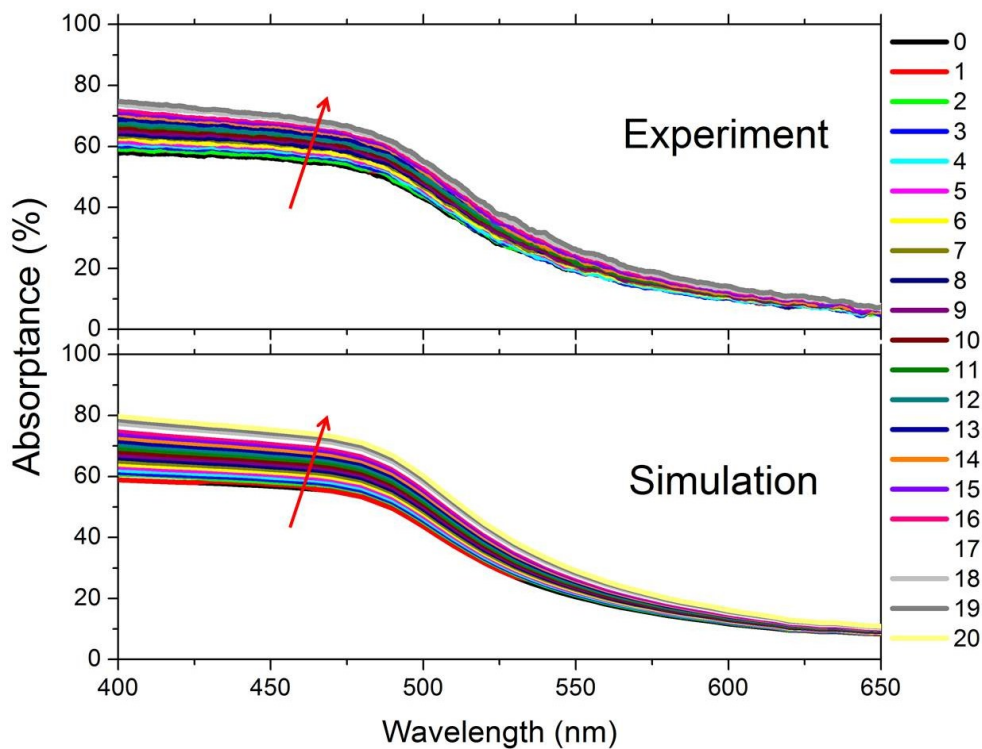
Figure 5.1. Experiment and simulation results for the percent absorptance of 50 nm thick gold films coated with various thicknesses of Al₂O₃ ranging from 0 to 20 nm with 1 nm steps.
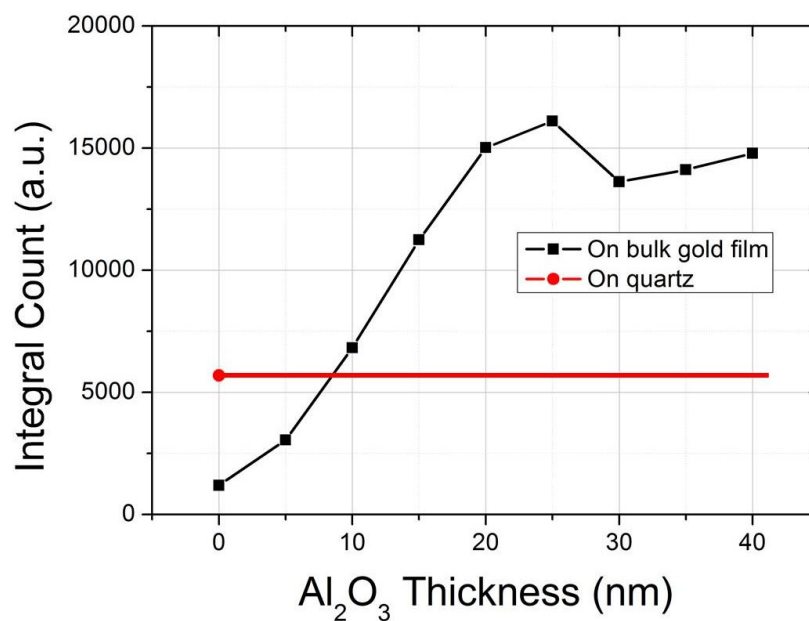
Figure 5.2. Metal enhanced fluorescence measurements of the giant QDs on Al₂O₃ deposited 50 nm thick gold films. As a negative control sample, QD PL intensity on the bare fused silica is indicated with a red line.

From Figure 5.2, we observe that 10 nm oxide layer is almost the same with the giant QD emission intensity on the fused silica. Coating 10 nm oxide layer on our structure will ensure the fair comparison between the emissions of QDs on flat gold film outside the checkerboard structure and QDs on fused silica, eliminating the enhanced fluorescence due to metal enhanced fluorescence. QDs are spin-coated at 3000 rpm for 3 min on the checkerboard structures. Figure 5.3 shows the SEM image of the coated QDs on the checkerboard structures. The SEM images indicated that QDs are coated quite successfully in terms of homogeneity and having near-unity surface coverage.
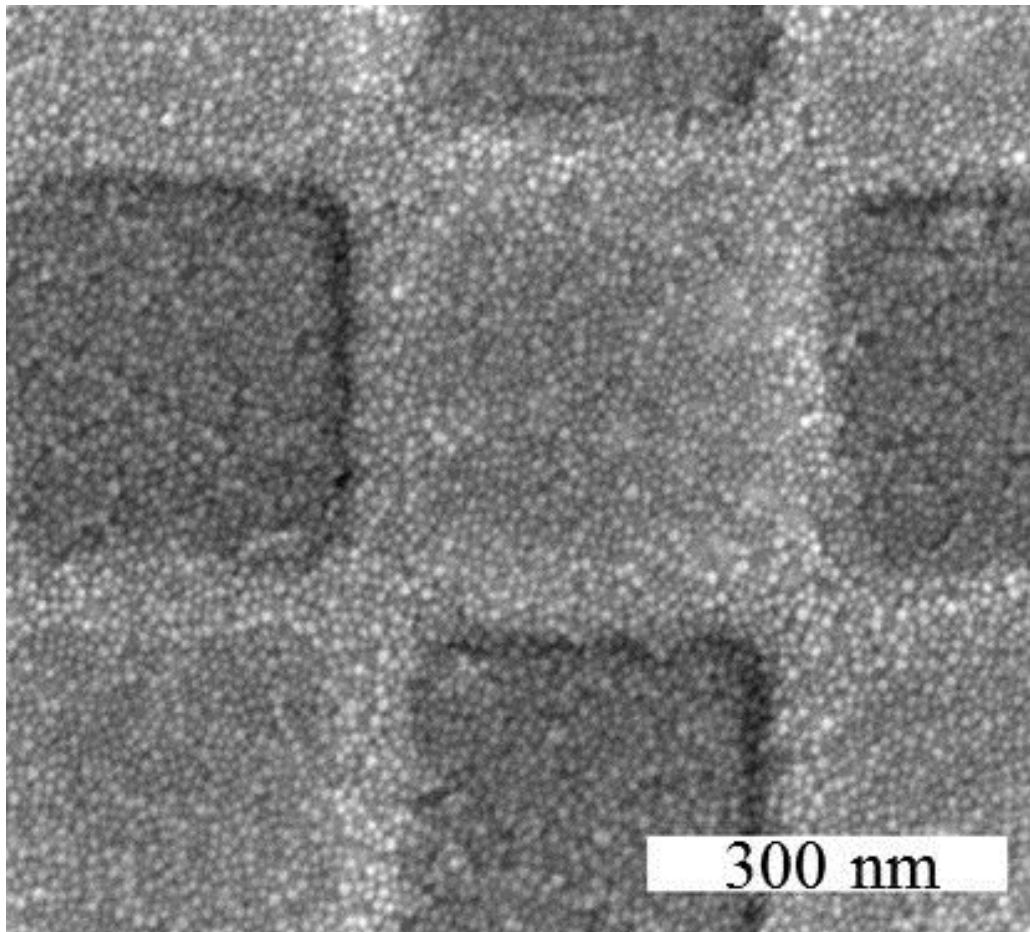
Figure 5.3. Giant QD coated 3D checkerboard structure with a scalebar corresponding to 300 nm length.

Photoluminescence maps of the giant QD coated 3D checkerboard structure are obtained using confocal microscopy with 20X objective. Results showing the maps of PL emission intensity and PL emission peak wavelength are presented in Figure 5.4. PL intensities are normalized with respect to the maximum PL emission signal on the 3D checkerboard structure. A 5.4-fold emission enhancement is observed in the 3D structure with respect to the bulk gold film. This obtained value is comparable to the observed field enhancement value from the simulations having about 8-fold field enhancement observed in Figure 3.3.1 for the 3D structure.

The advantage of the 3D checkerboard structure reveals itself in time-resolved fluorescence measurements. TRF measurements are taken with the giant QDs spin-coated on the 3D structure with 10 nm aluminum oxide deposited on it. From Figure 5.5 we observe that the amplitude averaged decay lifetime of QDs on continuous gold film decreases compared to the 3D checkerboard structure from 4.6 to 2.7 ns. However, photon counts reaching PMT increases from 2,700 to 25,000 counts for the 3D structure compared to the continuous gold film. At the optimum plasmonic coupling distance, the 3D structure effectively increases the radiative channels, resulting in increased PL intensity, while the continuous bulk film effectively increases the nonradiative channels. A 9.3-fold enhancement was observed in the TRF measurements of oblique configuration, which is different than the confocal measurements in normal configuration, possibly due to the angled illumination and collection geometry of the TRF measurement.
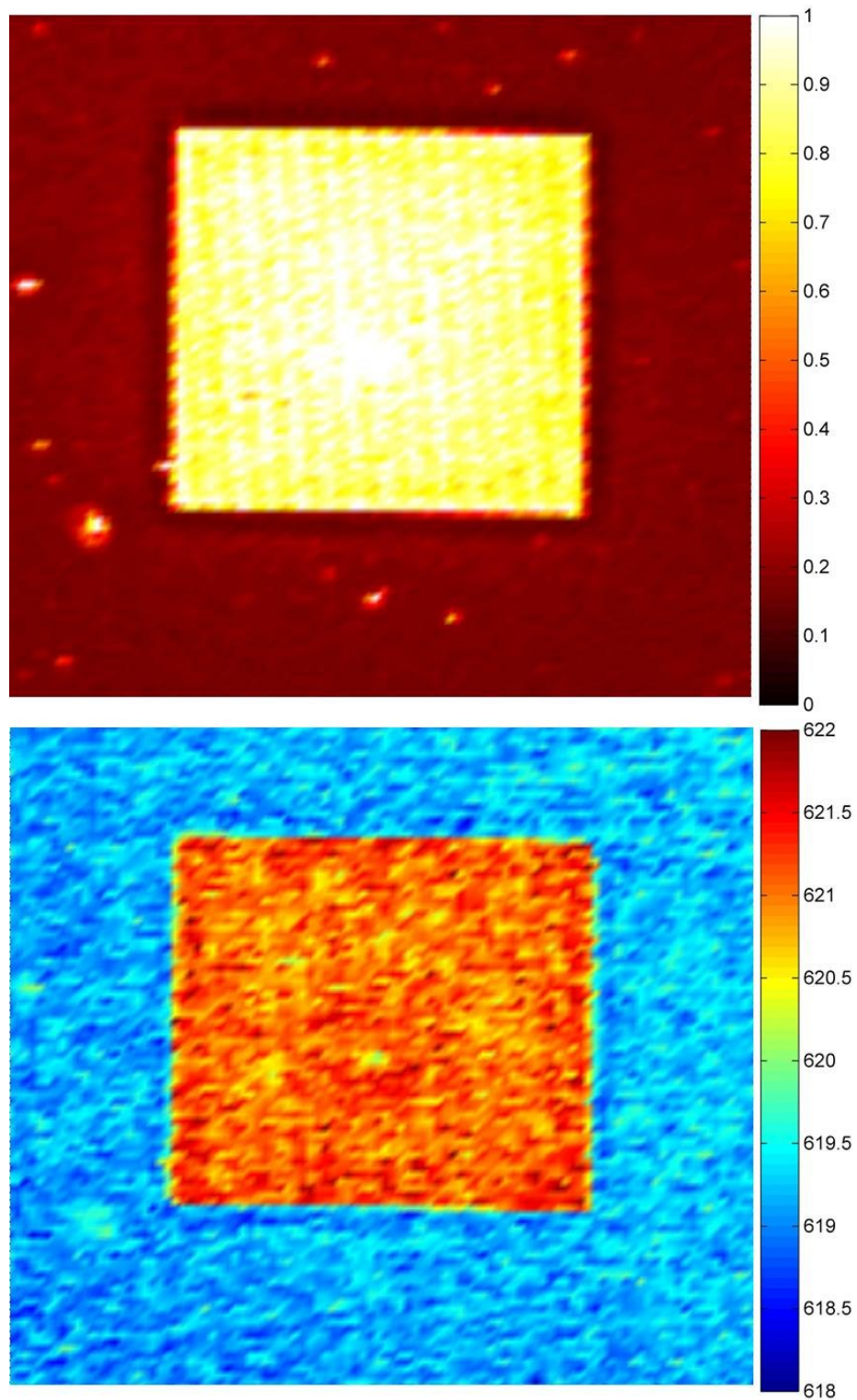
Figure 5.4. Giant QD coated 3D checkerboard structure: PL emission intensity map normalized to maximum intensity observed (top) and peak emission wavelength of QDs on the given structure with colorbar representing wavelengths in nm scale (bottom).
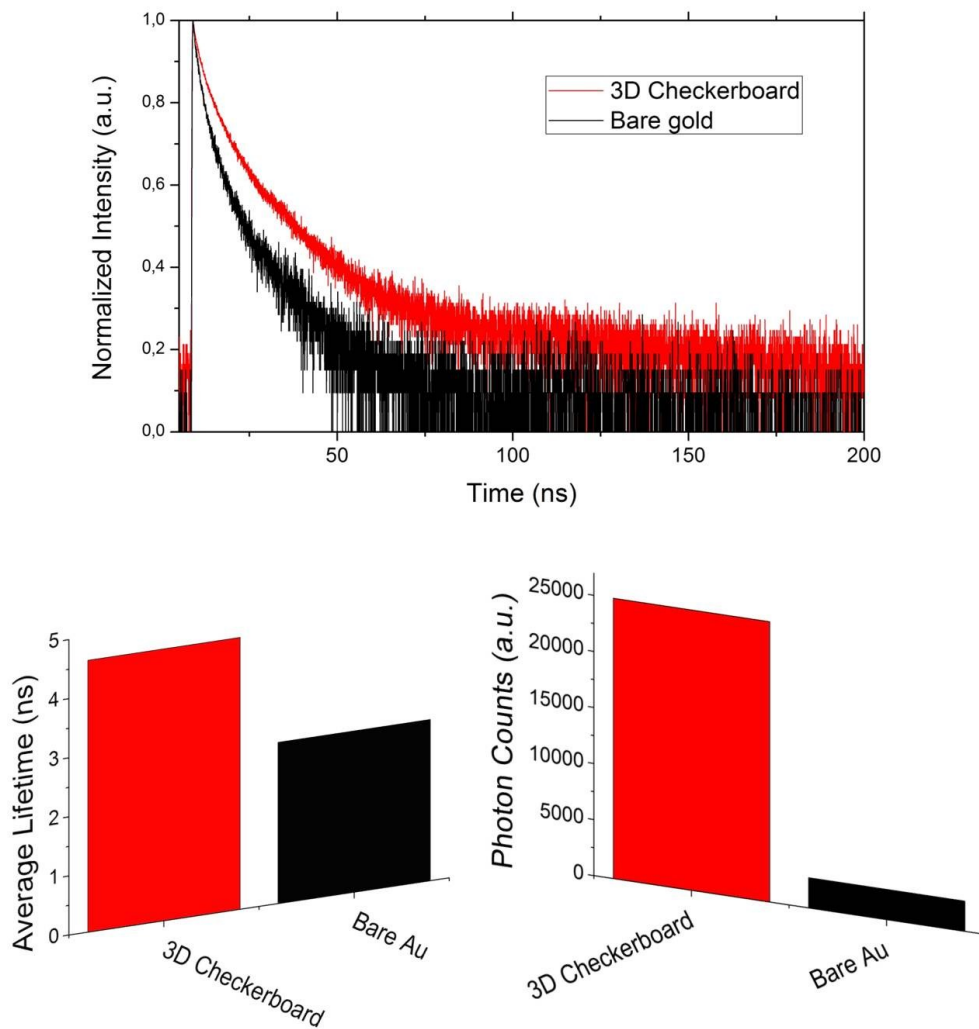
Figure 5.5. Time-resolved fluorescence measurements of giant QDs on our 3D checkerboard structure with respect to the bare gold film, both with 10 nm separating oxide layer.

Conclusions and Future Directions

In this thesis work, we worked on the problem limited of field enhancement nature of conventional two-dimensional plasmonic structures by proposing and developing three-dimensional plasmonic surfaces. Unlike the three-dimensional plasmonic structures found in the literature, our method introduces fewer fabrication steps than any structure produced using electron beam lithography technique. As inherently having unity surface coverage in plan view, 3D plasmonic surfaces exceed the performance of conventional 2D plasmonic structures. Also, coupling between two vertically separated complementary planes o the 3D structure creates out-of-plane plasmon modes which facilitates field enhancement into the free space stronger.

Theoretical analyses of the 2D and 3D checkerboards were performed using finite difference time domain method. Out-of-plane mode of the 3D checkerboard was examined using two complementary planes named as the upper and lower planes with respect to their positions. Out-of-plane mode is present in the upper plane surface; however, having coupled to the lower plane, the 3D structure shows a stronger resonance and field enhancement. We also approached plasmonic structures as a grating structure with similar periodicity properties and observed the nature of in-plane and out-of-plane modes clearly from the electric field intensity maps at the resonances of 2D and 3D structures, respectively. As a result, we observed 7.2-fold stronger maximum field localization in the 3D structure compared to the 2D structure. In order to use our structure as an efficient field enhancer with an emitter without quenching, a dielectric spacer layer should be placed. The effect of the dielectric spacer layer is also observed with varying thicknesses in the absorptance enhancement of the 2D structure and resonance redshift in the 3D structure.

The proposed structures were fabricated using electron beam lithography and characterized both structurally and optically. The structural and optical measurements meet theoretical expectations successfully. The 3D structure shows the plasmonic resonance at around 580 nm in both simulations and experiments with similar quality factors obtained by the Lorentzian lineshape fit analysis.

Finally, as an application, we spin-coated colloidal giant quantum dots on 10 nm aluminum oxide coated 3D structure and obtained photoluminescence emission intensity map and time-resolved fluorescence results. We observed a 5.4-fold enhancement using confocal microscopy measurements on the 3D structure compared to the continuous gold film, which is comparable to numerically expected volumetric field enhancement around 8. In time-resolved fluorescence measurements, the enhancement factor reaches 9.3, which can be attributed to the collection geometry efficiency.

Future aspects for the three-dimensional surfaces includes coupling of novel complementary planes with stronger resonance to achieve higher enhancement factors to be used in device applications like light-emitting diodes. We believe that implementing large area and low cost fabrication methods such as nanoimprint lithography technique into the fabrication, the 3D nanoplasmonic surfaces are promising for high performance photonic devices.

Bibliography

[1]   S. Maier, M. Brongersma, P. Kik, and H. Atwater, "Observation of near-field coupling in metal nanoparticle chains using far-field polarization spectroscopy," *Physical Review B*, vol. 65, no. 19, pp. 1–4, May 2002.

[2]   B. V. E. Ferry, J. N. Munday, and H. A. Atwater, "Design Considerations for Plasmonic Photovoltaics," *Applied Physics*, pp. 4794–4808, 2010.

[3]   C. Sönnichsen, "Plasmons in metal nanostructures," Ludwig-Maximilians-Universität München, 2001.

[4]   A. Boltasseva and H. A. Atwater, "Low-loss plasmonic metamaterials," *Science*, vol. 331, pp. 290–1, 2011.

[5]   T. W. Ebbesen, H. J. Lezec, H. F. Ghaemi, T. Thio, and P. A. Wolff, "Extraordinary optical transmission through sub-wavelength hole arrays," *Nature*, vol. 391, no. 12, pp. 667–9, Feb. 1998.

[6]   K. Aydin, V. E. Ferry, R. M. Briggs, and H. a Atwater, "Broadband polarization-independent resonant light absorption using ultrathin plasmonic super absorbers.," *Nature Communications*, vol. 2, p. 517, Jan. 2011.

[7]   S. Gao, K. Ueno, and H. Misawa, "Plasmonic Antenna Effects on Photochemical Reactions," *Accounts of Chemical Research*, vol. 44, no. 4, pp. 251–260, 2011.

[8]   K. Ueno, S. Juodkazis, V. Mizeikis, K. Sasaki, and H. Misawa, "Clusters of Closely Spaced Gold Nanoparticles as a Source of Two-Photon Photoluminescence at Visible Wavelengths," *Advanced Materials*, vol. 20, no. 1, pp. 26–30, Jan. 2008.

[9]   J. Maria, T. T. Truong, J. Yao, T.-W. Lee, R. G. Nuzzo, S. Leyffer, S. K. Gray, and J. A. Rogers, "Optimization of 3D plasmonic crystal structures for refractive index sensing," *J. Phys. Chem. C*, vol. 113, no. 24, pp. 10493–10499, 2009.

[10]   J. Xu, P. Guan, P. Kvasni, H. Gong, and Q. Yu, "Light Transmission and Surface-Enhanced Raman Scattering of Quasi-3D Plasmonic Nanostructure Arrays with Deep and rot Nanocavities Shallow Fabry-Pérot Nanocavities," *Journal of Physical Chemistry C*, no. 115, pp. 10996–11002, 2011.

[11]   Q. Yu, P. Guan, D. Qin, G. Golden, and P. M. Wallace, "Inverted size-dependence of surface-enhanced Raman scattering on gold nanohole and nanodisk arrays.," *Nano Letters*, vol. 8, no. 7, pp. 1923–8, Jul. 2008.

[12]   Y. Yokota, K. Ueno, S. Juodkazis, V. Mizeikis, N. Murazawa, H. Misawa, H. Kasa, K. Kintaka, and J. Nishii, "Nano-textured metallic surfaces for optical sensing and detection applications," *Journal of Photochemistry and Photobiology A: Chemistry*, vol. 207, no. 1, pp. 126–134, Sep. 2009.

[13]   Q. Yu, S. Braswell, B. Christin, and J. Xu, "Surface-enhanced Raman scattering on gold quasi-3D nanostructure and 2D nanohole arrays," *Nanotechnology*, vol. 21, no. 355301, 2010.

[14]   T. Ozel, I. M. Soganci, S. Nizamoglu, I. O. Huyal, E. Mutlugun, S. Sapra, N. Gaponik, A. Eychmüller, and H. V. Demir, "Selective enhancement of surface-state emission and simultaneous quenching of interband transition in white-luminophor CdS nanocrystals using localized plasmon coupling," *New Journal of Physics*, vol. 10, no. 8, p. 083035, Aug. 2008.

[15]   I. M. Soganci, S. Nizamoglu, E. Mutlugun, O. Akin, and H. V Demir, "Localized plasmon-engineered spontaneous emission of CdSe/ZnS

nanocrystals closely-packed in the proximity of Ag nanoisland films for controlling emission linewidth, peak, and intensity.," *Optics Express*, vol. 15, no. 22, pp. 14289–98, Oct. 2007.

[16]   O. Kulakovich, N. Strekal, A. Yaroshevich, S. Maskevich, S. Gaponenko, I. Nabiev, U. Woggon, and M. Artemyev, "Enhanced Luminescence of CdSe Quantum Dots on Gold Colloids," *Nano Letters*, vol. 2, no. 12, pp. 1449–1452, Dec. 2002.

[17]   T. Ozel, S. Nizamoglu, M. A. Sefunc, O. Samarskaya, I. O. Ozel, E. Mutlugun, V. Lesnyak, N. Gaponik, A. Eychmuller, and S. V Gaponenko, "Anisotropic Emission from Multilayered Plasmon Resonator Nanocomposites of Isotropic Semiconductor Quantum Dots," *ACS Nano*, vol. 5, no. 2, pp. 1328–1334, 2011.

[18]   P. P. Pompa, L. Martiradonna, a Della Torre, F. Della Sala, L. Manna, M. De Vittorio, F. Calabi, R. Cingolani, and R. Rinaldi, "Metal-enhanced fluorescence of colloidal nanocrystals with nanoscale control.," *Nature Nanotechnology*, vol. 1, no. 2, pp. 126–30, Nov. 2006.

[19]   E. Hwang, I. I. Smolyaninov, and C. C. Davis, "Surface plasmon polariton enhanced fluorescence from quantum dots on nanostructured metal surfaces.," *Nano Letters*, vol. 10, no. 3, pp. 813–20, Mar. 2010.

[20]   J.-H. Song, T. Atay, S. Shi, H. Urabe, and A. V Nurmikko, "Large enhancement of fluorescence efficiency from CdSe/ZnS quantum dots induced by resonant coupling to spatially controlled surface plasmons.," *Nano Letters*, vol. 5, no. 8, pp. 1557–61, Aug. 2005.

[21]   Y. Jiang, H.-Y. Wang, H. Wang, B.-R. Gao, Y. Hao, Y. Jin, Q.-D. Chen, and H.-B. Sun, "Surface Plasmon Enhanced Fluorescence of Dye Molecules on Metal Grating Films," *Journal of Physical Chemistry C*, vol. 115, no. 25, pp. 12636–12642, Jun. 2011.

[22] "The Lycurgus Cup." [Online]. Available: http://www.britishmuseum.org/explore/highlights/highlight_objects/pe_m la/t/the_lycurgus_cup.aspx.

[23] P. L. Stiles, J. a Dieringer, N. C. Shah, and R. P. Van Duyne, "Surface-enhanced Raman spectroscopy.," *Annual Review of Analytical Chemistry (Palo Alto, Calif.)*, vol. 1, pp. 601–26, Jan. 2008.

[24] S. V Gaponenko, *Introduction to Nanophotonics*. Cambridge: Cambridge University Press, 2010.

[25] W. U. Huynh, J. J. Dittmer, and a P. Alivisatos, "Hybrid nanorod-polymer solar cells.," *Science (New York, N.Y.)*, vol. 295, no. 5564, pp. 2425–7, Mar. 2002.

[26] Y.-H. Su, Y.-F. Ke, S.-L. Cai, and Q.-Y. Yao, "Surface plasmon resonance of layer-by-layer gold nanoparticles induced photoelectric current in environmentally-friendly plasmon-sensitized solar cell," *Light: Science & Applications*, vol. 1, no. 6, p. e14, Jun. 2012.

[27] B. O. Dabbousi, M. G. Bawendi, O. Onitsuka, and M. F. Rubner, "Electroluminescence from CdSe quantum-dot/polymer composites," *Applied Physics Letters*, vol. 66, no. 11, p. 1316, 1995.

[28] V. I. Klimov, "Optical Gain and Stimulated Emission in Nanocrystal Quantum Dots," *Science*, vol. 290, no. 5490, pp. 314–317, Oct. 2000.

[29] S. Maier, *Plasmonics: fundamentals and applications*. Springer, 2007.

[30] C. Kittel, *Introduction to Solid State Physics*, 8th ed. New York: John Wiley & Sons, 2005, p. 704.

[31] S. P. Apell, P. M. Echenique, and R. H. Ritchie, "Sum rules for surface plasmon frequencies," *Ultramicroscopy*, vol. 65, no. 1–2, pp. 53–60, Sep. 1996.

[32] C. Powell and J. Swan, "Effect of oxidation on the characteristic loss spectra of aluminum and magnesium," *Physical Review*, vol. 118, no. 3, pp. 640–643, 1960.

[33] R. H., *Surface Plasmons on Smooth and Rough Surfaces and on Gratings*. Berlin: Springer-Verlag, 1988.

[34] G. Mie, "Contributions to the optics of turbid media, particularly of colloidal metal solutions," *Ann Phys*, vol. 25, pp. 377–442, 1908.

[35] C. F. Bohren and D. R. Huffman, *Absorption and scattering of light by small particles*. Wiley, 1983.

[36] K. Kelly and E. Coronado, "The optical properties of metal nanoparticles: the influence of size, shape, and dielectric environment," *Journal of Physical Chemistry B*, pp. 668–677, 2003.

[37] L. Novotny and B. Hecht, *Principles of nano-optics*. New York: Cambridge University Press, 2006.

[38] J. Clarkson, "Plasmon Enhanced Absorption in Photovoltaic Cells," University of Rochester, 2010.

[39] S. Link, M. B. Mohamed, and M. a. El-Sayed, "Simulation of the Optical Absorption Spectra of Gold Nanorods as a Function of Their Aspect Ratio and the Effect of the Medium Dielectric Constant," *Journal of Physical Chemistry B*, vol. 103, no. 16, pp. 3073–3077, Apr. 1999.

[40] H. Kuwata, H. Tamaru, K. Esumi, and K. Miyano, "Resonant light scattering from metal nanoparticles: Practical analysis beyond Rayleigh approximation," *Applied Physics Letters*, vol. 83, no. 22, p. 4625, 2003.

[41] A. P. Alivisatos, "Perspectives on the Physical Chemistry of Semiconductor Nanocrystals," *Journal of Physical Chemistry,* vol. 3654, no. 95, pp. 13226–13239, 1996.

[42] Y. Chen, J. Vela, H. Htoon, J. L. Casson, D. J. Werder, D. a Bussian, V. I. Klimov, and J. a Hollingsworth, "'Giant' multishell CdSe nanocrystal quantum dots with suppressed blinking.," *Journal of the American Chemical Society*, vol. 130, no. 15, pp. 5026–7, Apr. 2008.

[43] M. A. Sefunc, A. K. Okyay, and H. V. Demir, "Volumetric plasmonic resonator architecture for thin-film solar cells," *Applied Physics Letters*, vol. 98, no. 9, p. 093117, 2011.

[44] R. a. Pala, J. White, E. Barnard, J. Liu, and M. L. Brongersma, "Design of Plasmonic Thin-Film Solar Cells with Broadband Absorption Enhancements," *Advanced Materials*, vol. 21, no. 34, pp. 3504–3509, Sep. 2009.

[45] J. M. Taboada, J. Rivero, F. Obelleiro, M. G. Araújo, and L. Landesa, "Method-of-moments formulation for the analysis of plasmonic nano-optical antennas.," *Journal of the Optical Society of America. A, Optics, image science, and vision*, vol. 28, no. 7, pp. 1341–8, Jul. 2011.

[46] P. K. Jain, S. Eustis, and M. a El-Sayed, "Plasmon coupling in nanorod assemblies: optical absorption, discrete dipole approximation simulation, and exciton-coupling model.," *Journal of Physical Chemistry. B*, vol. 110, no. 37, pp. 18243–53, Sep. 2006.

[47] N. Félidj, J. Aubard, and G. Lévi, "Discrete dipole approximation for ultraviolet–visible extinction spectra simulation of silver and gold colloids," *Journal of Chemical Physics*, vol. 111, no. 3, p. 1195, 1999.

[48] P. Johnson and R. Christy, "Optical constants of the noble metals," *Physical Review B*, vol. 1318, no. 1970, 1972.

[49] E. M. Purcell, "Spontaneous Emission Probabilities at Radio Frequecies," *Physical Review*, vol. 69, no. 11–12, p. 674, 1946.

[50] Q. Hang, D. a. Hill, and G. H. Bernstein, "Efficient removers for poly(methylmethacrylate)," *Journal of Vacuum Science & Technology B: Microelectronics and Nanometer Structures*, vol. 21, no. 1, p. 91, 2003.

[51] S. Gieraltowska and D. Sztenkiel, "Properties and characterization of ALD grown dielectric oxides for MIS structures," *Acta Physica Polonica A*, 2010, vol. 119, no. 5, pp. 692–695.